

Cutting corners to suppress high-order modes in Mie resonator arrays

Zaid Haddadin¹, Shahrose Khan², and Lisa V. Poulikakos^{*2,3}

¹Department of Electrical & Computer Engineering, UC San Diego

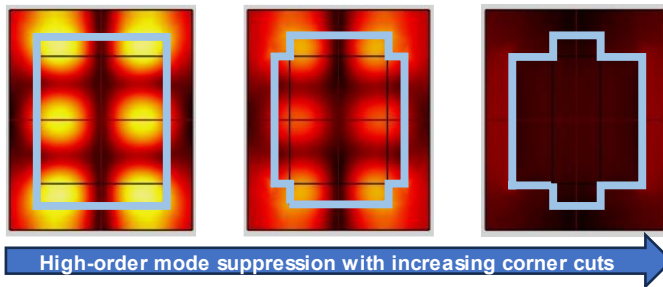
²Department of Mechanical & Aerospace Engineering, UC San Diego

³Materials Science & Engineering Program, UC San Diego

Keywords: lattice, resonances, metasurfaces, saturation, silicon nitride, structural colour,

ABSTRACT: Mie resonators as lattice resonant metasurfaces have the capability to produce structural colour. However, design criteria for these metasurfaces are still being investigated. In this work, we numerically examine how the two-dimensional nanostructure shape in a lattice array affects the colorimetric response of the metasurface under linearly polarised light excitation. First, the transformation from a square-shaped to rectangle-shaped nanostructure array resulted in polarisation-sensitive metasurfaces with colorimetric outputs bound along a line on the CIE 1931 2-degree Standard Observer colour space. The bounds of the colorimetry line were tuneable to any desired chromatic range. Second, the removal of the corners in square- or rectangle-shaped nanostructures to create t-shaped nanostructure arrays displayed a dampening effect on the high-order resonance. Finally, we analytically determined that the colour saturation could increase when moving from rectangle-shaped to t-shaped nanostructure arrays. From these results, we present two design guidelines for lattice resonant metasurfaces: (1) Constructing the nanostructure to support fundamental resonances at different wavelengths enables two-colour-bound movement when excited by successive angles of linearly polarised light; (2) Removing portions of the nanostructure that only support high-order resonances dampens these modes while maintaining support for fundamental resonances. These results present first-principles guidelines for engineering nanoparticles in lattice resonant metasurfaces, offering a new toolbox for polarised-light sensing and colorimetric applications.

TOC Graphic



Introduction

Structural colour arises from the scattering, diffraction, and dispersion of light by interactions with subwavelength structures¹⁻⁸, which result from interference effects between electromagnetic waves and matter^{9,10}. Other mechanisms for colour generation include light absorption, transmission, and reflection by pigments¹¹⁻¹³, which can exhibit instability¹⁴⁻¹⁷; and light emission through luminescence¹⁸⁻²⁰, which can be limited in duration and intensity²⁰.

Structural colours offer vivid saturations with enhanced resolution, tunability, and durability compared to their chemical counterparts¹⁰. They have been studied since initial observations by Robert Hooke²¹ and Isaac Newton²². Research has explored the generation of structural colours

for various applications: biomedical sensing²³⁻³², coloured displays³²⁻³⁴, solar energy conversion³⁵⁻³⁷, information encryption^{38,39}, and more⁴⁰⁻⁴². However, full realisation of these applications necessitates a deeper understanding of the mechanisms enabling control and tunability of colour saturation, resonant wavelength, and colorimetric multiplexing.

Metasurfaces – engineered periodic arrangements of sub-wavelength nanostructures – offer efficient, tuneable systems for generating structural colour. These colorimetric metasurfaces can consist of (i) plasmonic⁴³⁻⁴⁶, (ii) dielectric⁴⁷⁻⁵¹, or (iii) hybrid⁵²⁻⁶⁰ material systems. Plasmonic systems – including hybrid systems with plasmonic materials – suffer high optical losses in the visible light regime, limiting production of saturated structural colours⁶¹⁻⁶³. In contrast, dielectric materials, which can exhibit low dissipative losses and medium-to-high refractive indices, serve as efficient generators of structural colour⁶⁴⁻⁶⁶.

Dielectric structures can support Mie resonances, which depend on the size and geometry of the particles interacting with incident electromagnetic waves⁶⁷⁻⁷⁰. Structural colour can be achieved by tuning the geometry of the dielectric particle to confine the resonance within the visible light regime⁷¹. The effect was attributed to magnetic dipole excitation in 2012^{67,68}. Since then, research has explored how arrays of dielectric nanostructure elements, known as all-dielectric metasurfaces, can achieve colour filtering^{72,73}.

All-dielectric colorimetric metasurfaces have been demonstrated using one-dimensional subwavelength features, such as gratings⁷⁴, or using two-dimensional subwavelength features in the form of periodically arranged nanoparticles⁷⁵. In the latter case, the periodic repetition of subwavelength Mie scatterers enhances the magnetic dipole excitation compared to the single particle case, because of the collective resonant nature of a lattice array^{76–86}. Alterations to the periodicity of the lattice array through structural adjustments of the particles and/or changes to the spacing among particles can modify the resonant wavelength^{84–86}.

This lattice resonant effect has been utilised to generate structural colours in reflectance using square-shaped nanostructure arrays made of silicon nitride⁴⁷. Although a dampening effect on high-order Mie resonances was observed while preserving the fundamental resonance, the presence of high-order resonances in structures generating red colour was still reported⁴⁷. Consequently, the design of nanostructure arrays that eliminate support for high-order Mie resonances remains an unanswered question.

This work introduces new criteria for the design of nanostructure arrays aimed at dampening or extinguishing high-order resonances. Finite element method simulations were conducted to study square- and rectangle-shaped nanostructure arrays. The rectangle-shaped nanostructure arrays demonstrated two distinct structural colour outputs in reflectance when excited by linearly polarised light aligned with either the vertical or horizontal axis; this is attributed to the separate Mie resonances arising from the different periodicities along those axes^{83,86}. When the linearly polarised light was inclined towards or away from these orthogonal axes, a hybrid signal comprising amplitude-adjusted components of vertically and horizontally polarised light was observed. The resulting structural colour output of these hybrid signals was plotted along a line, bounded by two colours, on the CIE 1931 2-degree Standard Observer colour space^{87,88}. The bounds of the colorimetry line were shown to be tuneable to any desired range, such as but not limited to blue-green, blue-red, and green-red.

The examination of near-field effects in the lattice arrays led to the hypothesis that removal of specific sections in the nanostructures that solely contribute to high-order resonances would dampen or extinguish them. In this work, the corners of the nanostructures met this criterion and removing them led to the predicted outcome. When the corners were removed without destabilising the fundamental resonances, the analytically calculated colour saturations increased. These findings emphasise how the intentional design of nanoparticles to selectively suppress or enable resonant modes offers an additional degree of freedom for tuning metasurfaces in polarised light-sensing applications.

Results & Discussion

Lattice arrays consisting of silicon nitride particles on a silicon dioxide substrate were modelled in COMSOL Multiphysics® v5.6⁸⁹, a finite element method simulation software, using the Wave Optics module⁹⁰ and solved at the

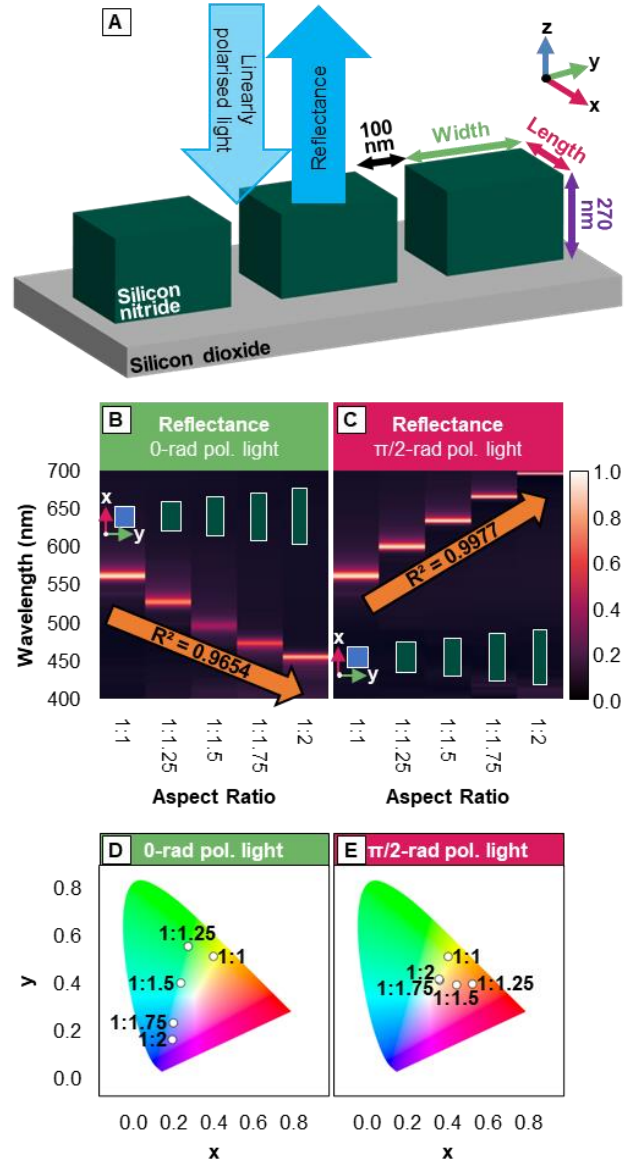


Figure 1. (A) Schematic of lattice resonant metasurface comprised of rectangle-shaped, silicon nitride nanostructures on a silicon dioxide substrate. (B,C) Heatmaps showing reflectance spectra of varying aspect ratios of rectangle-shaped nanostructure arrays acquired by excitation with (B) 0 rad (y-axis) or (C) $\pi/2$ rad (x-axis) linearly polarised light, illustrating the linear relationship between width or length of the nanostructure and the resonant wavelength. (D,E) Colorimetric outputs predicted from each reflectance spectra in (B) and (C) plotted on the CIE 1931 2-degree Standard Observer colour space, illustrating movement from green-to-blue when shortening the rectangle width and green-to-red when increasing the rectangle length.

San Diego Supercomputer Center⁹¹. These arrays were designed with Floquet periodicity conditions (see Supplementary Material, Section S1 for implementation details). Each particle had a fixed height of 270 nm, and the gap among particles was held at 100 nm (Figure 1A). The two-dimensional shape, width, and length of the nanoparticles were varied across arrays. The tested shapes included rectangles and t-shaped configurations, where t-shapes represent rectangles with the corners removed. The periodicity

ty along the y-axis (or x-axis) was calculated by [width (or length) + 100 nm]. Linearly polarised light was used to excite the nanostructure arrays at angles of 0 rad (y-axis polarised), $\pi/6$ rad, $\pi/4$ rad, $\pi/3$ rad, and $\pi/2$ rad (x-axis polarised). Reflectance data and near-field electric and magnetic field norm data were obtained for each study using the built-in functions of COMSOL Multiphysics® v5.6⁸⁹. The generated reflectance spectra were utilised to predict the structural colour output on the CIE 1931 2-degree Standard Observer colour space^{87,88} (see Supplementary Material, Section S2 for colour predicting calculations). These calculated structural colour outputs were converted to the CIE L*a*b* colour space^{92,93} to determine the colour saturation as a ratio of chroma to lightness⁹⁴⁻⁹⁷ (see Supplementary Material, Section S3 for colour saturation calculations).

An increase in aspect ratio from 1:1 to 1:2 with constant volume in rectangle-shaped nanostructure arrays (see Supplementary Material, Section S4 for parameters) resulted in a linear blue-shift in resonance location when excited with linearly polarised light at the 0 rad angle (Figure 1B) and a linear red-shift in resonance location when excited with light polarised at the $\pi/2$ rad angle (Figure 1C). These linear blue- and red-shifts had R^2 values of 0.9654 and 0.9977, respectively. These shifts corresponded to chromatic movements from green to blue in the former case (Figure 1D) and from green to red in the latter case (Figure 1E) on the CIE 1931 2-degree Standard Ob-

server colour space^{87,88}.

When maintaining a constant aspect ratio of 1:1.25 and exciting the nanostructure with linearly polarised light oriented at the $\pi/6$ rad, $\pi/4$ rad, and $\pi/3$ rad angles, hybrid signals of the resonances from the 0 rad and $\pi/2$ rad polarisations were observed (Figure 2A). These hybrid signals were amplitude-adjusted dependent on the angular deviation from the 0 rad or $\pi/2$ rad axes. The colorimetric output of these spectra appeared on a colorimetric line bounded by the outputs of the 0 rad and $\pi/2$ rad polarisations (Figure 2B). Examinations of the near-field plots at the resonant wavelength revealed a Mie lattice resonance and a magnetic dipole resonance (Figures 2C and 2D); electric field norm plots showed a coupling between the nanostructure and the substrate (Figure 2C); magnetic field norm plots displayed coupling among the nanostructures and between the nanostructure and substrate (Figure 2D). This is in accord with results previously reported⁴⁷.

However, some volumes of rectangle-shaped nanostructures displayed additional, unwanted resonances in the lattice array configurations. For example, a rectangle-shaped nanostructure with dimensions of 327.4-nm-by-247.5-nm displayed two resonant peaks when excited by linearly polarised light at 0 rad (Figure 3A): a high-order resonance at 432 nm with amplitude 0.73 and a fundamental resonance at 572 nm with amplitude 0.49. Analysis of

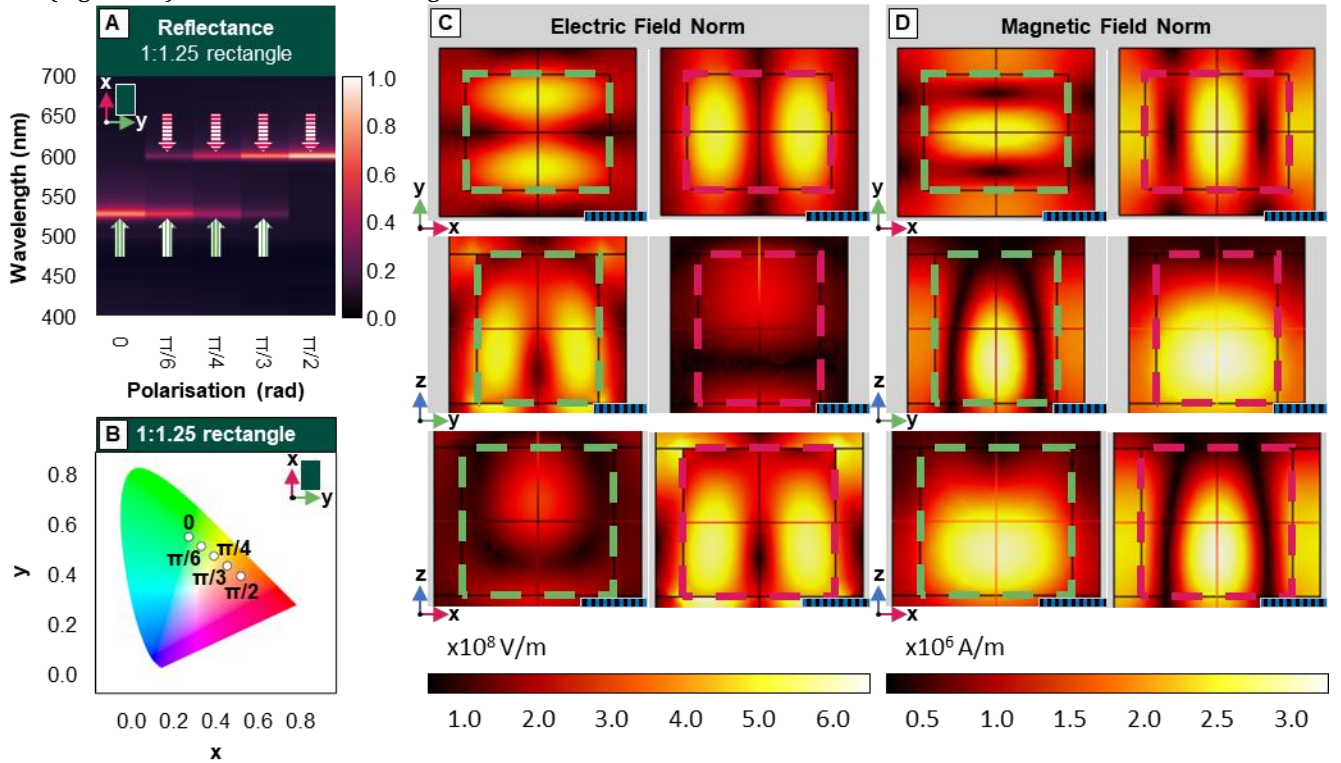


Figure 2. (A) Heatmap displaying reflectance spectra of a 1:1.25 aspect ratio rectangle excited by linearly polarised light at the 0 rad (y-axis), $\pi/6$ rad, $\pi/4$ rad, $\pi/3$ rad, and $\pi/2$ rad (x-axis) angles. Vertical, green-dashed arrows indicate the signal shared by the 0 rad polarisation resonance. Horizontal, red-dashed arrows indicate signal shared by $\pi/2$ rad polarisation resonance. (B) Colorimetric output predicted from each spectrum in (A) plotted on the CIE 1931 2-degree Standard Observer colour space. (C,D) Near-field (C) electric and (D) magnetic norm plots of the 1:1.25 aspect ratio rectangle excited by linearly polarised light along the (Left Column) 0 rad and (Right Column) $\pi/2$ rad angles. Dashed green or pink lines highlight the nanostructure boundary. Blue-and-black striped scale bars represent 100 nm.

the electric field norms at the high-order and fundamental resonance wavelengths revealed that the corners of the nanostructure supported nodes belonging to the high-order resonance but not the fundamental resonance (Figure 3B). To destabilise the support of the high-order resonance, the corners of the rectangle-shaped nanostructures were cut to create our first t-shaped nanostructure array with arm thicknesses of 247.5 nm and 187.1 nm (Figure 3C, Inset). With this new structure, the high-order reso-

nance in the reflectance spectrum was blue-shifted to 421 nm with a dampened amplitude of 0.38 (Figure 3C); the fundamental resonance blue-shifted to 567 nm with a maintained amplitude of 0.50. The near-field examinations at the high-order resonance wavelength showed a decrease in the maximum electric field norm value from $7.84\text{E}8$ V/m with the rectangle-shaped nanostructure array to $6.58\text{E}8$ V/m in the t-shaped nanostructure array (Figure 3D); the maximum electric field norm values at the

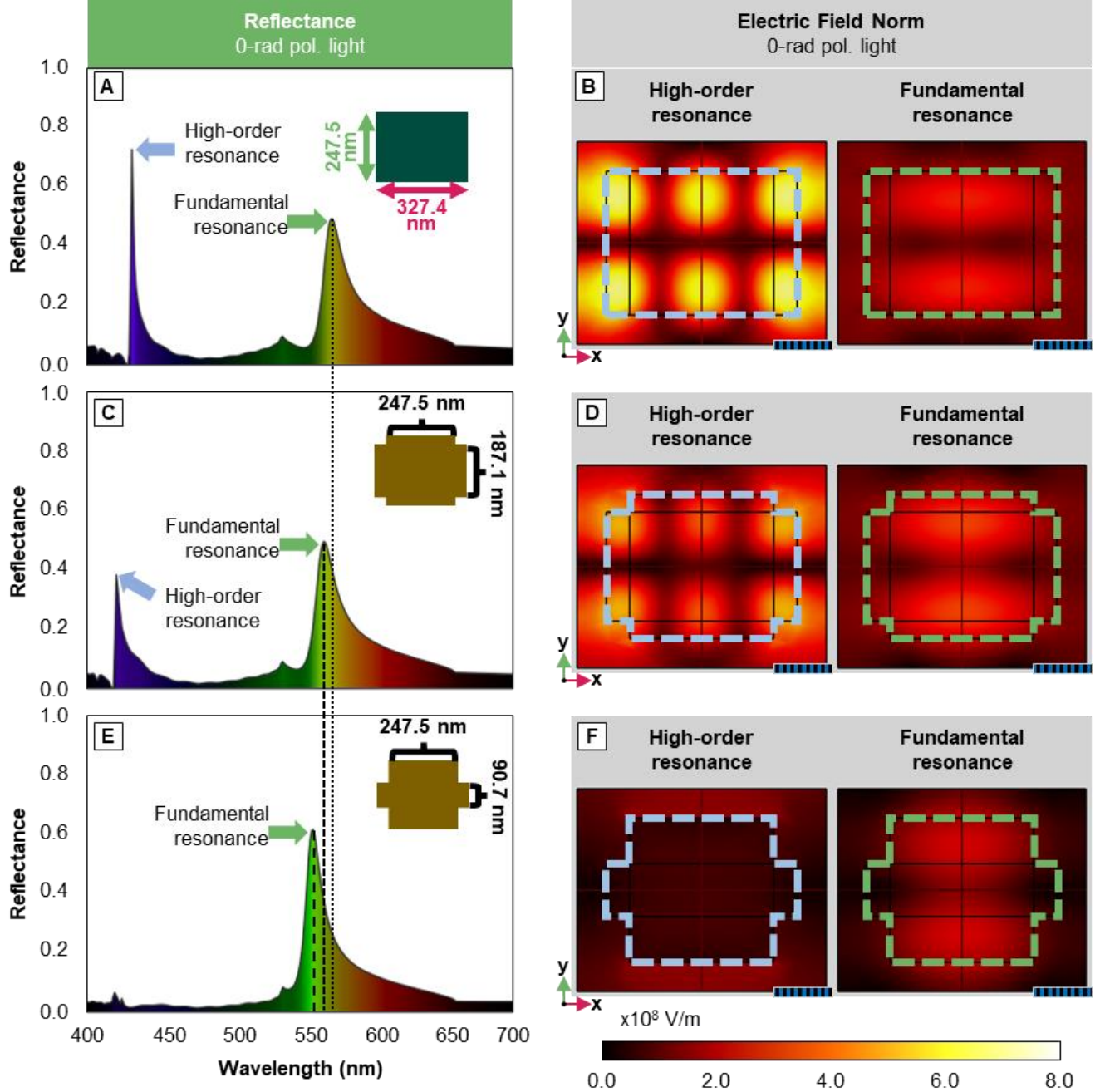


Figure 3. (A,C,E) Reflectance spectra of rectangle-shaped and t-shaped nanostructure arrays, indicated by insets, under linearly polarised light excitation at 0 rad (y-axis). Green arrows highlight the location of the fundamental resonance wavelength. Blue arrows highlight the location of the high-order resonance wavelength. The dotted, short dashed, and long dashed lines indicate the positions of the fundamental resonance wavelengths, which underwent a blue-shift when transforming a rectangle-shaped nanostructure array to a t-shaped nanostructure array. (B,D,F) Near-field plots of the electric norms of the (Left Column) high-order and (Right Column) fundamental resonances of the rectangle-shaped and t-shaped nanostructure arrays. Blue-and-black striped scale bars are 100 nm.

fundamental resonance differed by 0.01E8 V/m. To completely suppress the high-order resonance, a larger corner cut had to be made to create a second t-shaped nanostructure array with arm thicknesses of 247.5 nm and 90.7 nm (Figure 3E, Inset). Herein, the high-order resonance disappeared (Figure 3E); the fundamental resonance blue-shifted to 559 nm with an increased amplitude of 0.61. The maximum value of the electric field norm at the high-order resonance was 1.97E8 V/m (Figure 3F); the maximum value of the electric field norm at the fundamental resonance increased by 0.77E8 V/m, when compared with the rectangle-shaped nanostructure array result, to 4.39E8 V/m.

Overall, these cuts to the corners resulted in a suppressed high-order resonance, a blue-shifted fundamental resonance wavelength, an increased amplitude of the fundamental resonance wavelength, and an increased electric field norm magnitude of the fundamental resonance. We

hypothesise the blue-shift observed for the fundamental resonance wavelength can be minimised with appropriate increases to the effective dimension along the axis of polarisation – in this case, periodicity along the y-axis. We also noticed decreases to the full width at half-maximum of the fundamental resonance wavelength as the corners were cut (see Supplementary Material, Sections S5 and S6 for reported full widths at half-maximum and more examples of this phenomenon). When combining this observation with the increase in amplitude of the fundamental resonance wavelength in the second t-shaped nanostructure array, we can hypothesise there exists a trade-off between the available bandwidths for resonance formation and the peak intensity due to the laws of conservation. In addition, this sharpened resonance due to the decreased full width at half-maximum can improve the saturation of the colorimetric output resultant from the reflectance spectrum.

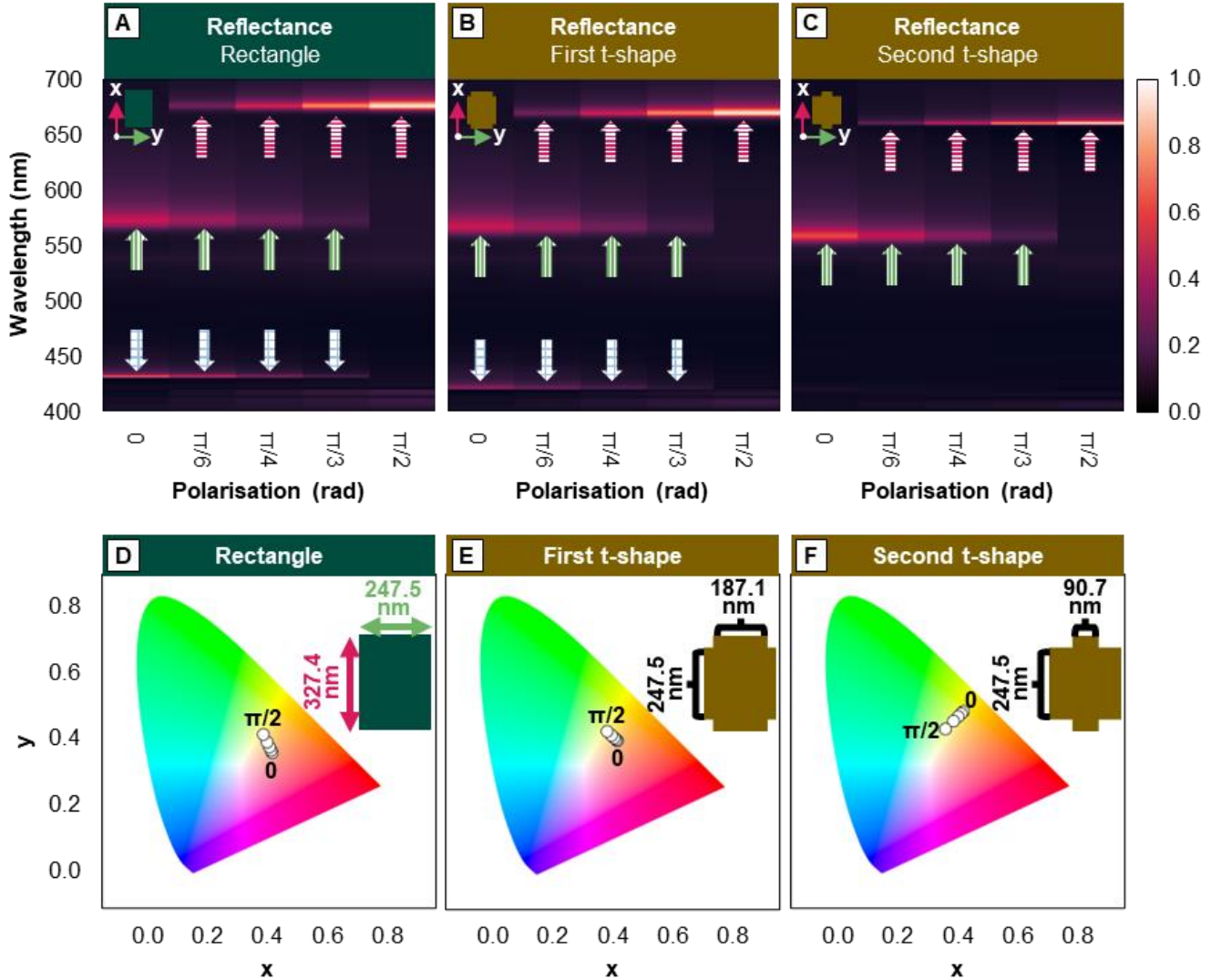


Figure 4. (A-C) Reflectance heatmaps acquired from the rectangle-shaped and t-shaped nanostructure arrays from Figure 3. Insets indicate the type of nanostructure. Blue, grid-filled arrows indicate the high-order resonances. Green, vertically striped arrows indicate fundamental resonance signals shared with the 0 rad (y-axis) polarisation. Red, horizontally striped arrows indicate fundamental resonance signals shared with the $\pi/2$ rad (x-axis) polarisation. The high-order resonances vanished with the t-shaped nanostructure array in (C). (D-F) Colorimetric output predicted from each reflectance spectrum in (A-C) plotted on the CIE 1931 2-degree Standard Observer colour space. Only the 0 rad (y-axis) and $\pi/2$ rad (x-axis) polarisations are labelled. All outputs are bounded along a line. The lines in (D, E) have a diagonal orientation. The line in (F) has an anti-diagonal orientation.

When exciting the rectangle-shaped, first t-shaped, and second t-shaped nanostructure arrays with linearly polarised light at the $\pi/6$ rad, $\pi/4$ rad, and $\pi/3$ rad angles, hybrid signals comprising the resonances from the 0 rad and $\pi/2$ rad polarisations were observed (Figure 4A-C). These hybrid signals were amplitude-adjusted based on angular deviation from the 0 rad or $\pi/2$ rad axes. The colorimetric output of these spectra on the CIE 1931 2-degree Standard Observer colour space^{87,88} appeared as a line bounded between the outputs of the 0 rad and $\pi/2$ rad polarisations (Figures 4D-F). If the colorimetry lines in Figures 4D and 4E were classified as oriented diagonally, then the colorimetry line in Figure 4F can be described as oriented anti-diagonally, closer to the edges of the colour space. Within this colour space, a tendency towards the edges represents a higher colour saturation^{9,72}, an indication that suppressing the high-order resonance impacts colorimetry. The colour saturation was calculated for all three lattice arrays when excited by linearly polarised light at 0 rad and $\pi/2$ rad (Figure 5). A greater range of increase in colour saturation was calculated under 0 rad polarisation compared to under $\pi/2$ rad polarisation when moving from the rectangle-shaped to the second t-shaped nanostructure arrays, an implication that suppression of the high-order resonance poses greater weighting on the final colour saturation than the decreased full widths at half-maximums of the resonance peaks. We chose to not conduct null hypothesis significant testing on the colour saturation calculations, because of the small sample sizes per category ($n=4$) and the numerical nature of this work provides a-priori knowledge that a colorimetric difference must exist if the

resonances in reflectance across spectra are different from one another. Consequently, our evaluations and conclusions of the colour saturations results are qualitative.

Conclusions

Based on the numerical studies conducted in this work, the following design criterion for nanostructures in lattice arrays can be identified: Removing sections of the nanostructure that solely contributed to high-order resonances dampened or extinguished those resonances while maintaining support for the fundamental resonances. This was established by investigating the near-field effects of the high-order and fundamental resonances of the rectangle-shaped nanostructure arrays. The high-order resonances exhibited activity at the corners and centres of the nanostructures, whereas the fundamental resonances only displayed activity at the centres of the nanostructures. Removal of the corners resulted in the dampening and extinction of the high-order resonance, as demonstrated in Figure 3.

This work reveals a new avenue for the design of nanostructures in lattice arrays. It holds potential in the development of two-colour-bound colorimetric sensors for incident linearly polarised light with rectangle-shaped-turned-t-shaped nanostructure arrays. And it can be extrapolated to the design of single-colour pixels using square-shaped-turned-t-shaped nanostructure arrays (see Supplementary Material, Section S6 for results and discussion). Moreover, t-shapes are not likely the sole type of shape transformation enabling the dampening of high-order resonances. Future research can explore optimisation techniques for selectively removing sections of nanostructures to destabilise high-order resonances while maintaining support for fundamental resonances. Our work removed all four corners of the rectangle-shaped structures, but investigating the effects of removing one, two, or three of the corners could yield new findings, especially when examining effects of asymmetric corner removal for creating chiral structures for the colorimetric sensing of incident clockwise and counterclockwise circularly polarised light without the need for circular dichroism setups⁹⁸. Finally, a question that emerged during this work is whether it would be possible to alter the nanostructures to exclusively support a fundamental resonance along a single axis. Achieving this would enable the design of polarisation-sensitive colour filters using lattice arrays.

Altogether, it was possible to determine a new methodology for designing lattice arrays by examining near-field effects and removing portions of the nanostructure that support unwanted resonances.

ASSOCIATED CONTENT

Supporting Information Available: The supplementary material text includes methods, calculations, additional data, details on the programming environments and scripts, and descriptions of all attached files. These files include the codes used to analyse the data of this work (see Supplementary Material, Section S7) and the data analysed in this published work (see Supplementary Material, Section S8). This material

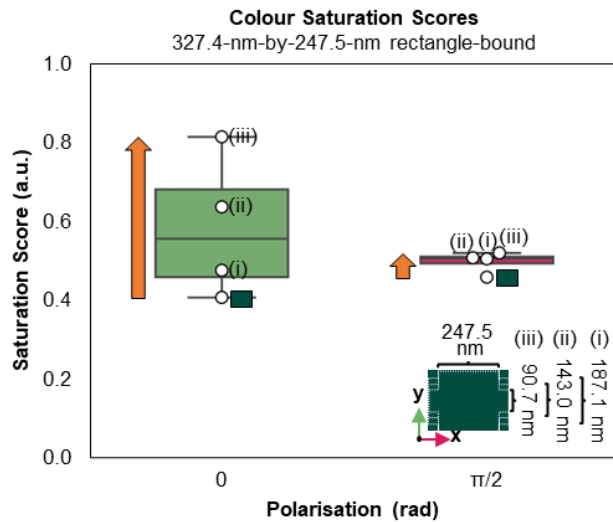


Figure 5. Box-and-whisker plot illustrating colour saturation measurements of rectangle-bound nanostructure arrays at 0 rad (y-axis) and $\pi/2$ rad (x-axis) linearly polarised light excitation. The green rectangle represents the control structure. (i), (ii), and (iii) indicate t-shape structures where (i) has the smallest area of corners removed and (iii) has the largest area of corners removed (exact dimensions provided in inset). Orange arrows indicate movement from the rectangle-shaped control to the t-shape with the greatest area of corners cut out. Boxes represent the quartiles, with the horizontal grey line indicating the median. Whiskers represent the range of the distribution.

is available free of charge via the Internet at <http://pubs.acs.org>.

AUTHOR INFORMATION

Corresponding Author

* L.V.P., University of California San Diego, La Jolla, CA, USA; lpoulidakos@ucsd.edu.

Author Contributions

Following CRediT definitions: conceptualisation: Z.H.; data curation: Z.H., S.K.; formal analysis: Z.H., S.K.; funding acquisition: L.V.P.; investigation: Z.H., S.K.; methodology: Z.H.; project administration: Z.H.; resources: L.V.P.; software: Z.H., S.K.; supervision: L.V.P.; validation: Z.H., S.K.; visualisation: Z.H., L.V.P.; writing – original draft: Z.H.; writing – review & editing: Z.H., S.K., L.V.P.

All authors have given approval to the final version of the manuscript.

Funding Sources

All authors gratefully acknowledge funding from the Arnold and Mabel Beckman Foundation (Beckman Young Investigator Award, Project Number: 30155266).

ACKNOWLEDGMENT

The authors thank Ping Chu, Subha Sivagnanam, and Dong-Chu “DJ” Choi for helpful discussions and technical support.

REFERENCES

- (1) Daqiqeh Rezaei, S.; Dong, Z.; You En Chan, J.; Trisno, J.; Ng, R. J. H.; Ruan, Q.; Qiu, C.-W.; Mortensen, N. A.; Yang, J. K. W. Nanophotonic Structural Colors. *ACS Photonics* **2021**, *8* (1), 18–33. <https://doi.org/10.1021/acsp Photonics.0c00947>.
- (2) Wu, L.; Cheng, K.; Lin, Y.-S. All-Dielectric Nanostructured Metasurfaces with Ultrahigh Color Purity and Selectivity for Reflective Index Sensing Applications. *Results in Physics* **2022**, *43*, 106092. <https://doi.org/10.1016/j.rinp.2022.106092>.
- (3) Xuan, Z.; Li, J.; Liu, Q.; Yi, F.; Wang, S.; Lu, W. Artificial Structural Colors and Applications. *The Innovation* **2021**, *2* (1), 100081. <https://doi.org/10.1016/j.xinn.2021.100081>.
- (4) Vukusic, P.; Sambles, J. R. Photonic Structures in Biology. *Nature* **2003**, *424* (6950), 852–855. <https://doi.org/10.1038/nature01941>.
- (5) Gur, D.; Leshem, B.; Pierantoni, M.; Farstey, V.; Oron, D.; Weiner, S.; Addadi, L. Structural Basis for the Brilliant Colors of the Sapphirinid Copepods. *J. Am. Chem. Soc.* **2015**, *137* (26), 8408–8411. <https://doi.org/10.1021/jacs.5b05289>.
- (6) Kinoshita, S.; Yoshioka, S.; Miyazaki, J. Physics of Structural Colors. *Rep. Prog. Phys.* **2008**, *71* (7), 076401. <https://doi.org/10.1088/0034-4885/71/7/076401>.
- (7) Seago, A. E.; Brady, P.; Vigneron, J.-P.; Schultz, T. D. Gold Bugs and beyond: A Review of Iridescence and Structural Colour Mechanisms in Beetles (Coleoptera). *J. R. Soc. Interface* **2009**, *6*, S165–S184. <https://doi.org/10.1098/rsif.2008.0354.focus>.
- (8) Vignolini, S.; Moyroud, E.; Glover, B. J.; Steiner, U. Analysing Photonic Structures in Plants. *Journal of The Royal Society Interface* **2013**, *10* (87), 20130394. <https://doi.org/10.1098/rsif.2013.0394>.
- (9) Wu, Y.; Chen, Y.; Song, Q.; Xiao, S. Dynamic Structural Colors Based on All-Dielectric Mie Resonators. *Advanced Optical Materials* **2021**, *9* (11), 2002126. <https://doi.org/10.1002/adom.202002126>.
- (10) Yang, B.; Cheng, H.; Chen, S.; Tian, J. Structural Colors in Metasurfaces: Principle, Design and Applications. *Mater. Chem.*

Front. **2019**, *3* (5), 750–761. <https://doi.org/10.1039/C9QM00043G>.

(11) Vogelmann, T. C.; Evans, J. R. Profiles of Light Absorption and Chlorophyll within Spinach Leaves from Chlorophyll Fluorescence. *Plant, Cell & Environment* **2002**, *25* (10), 1313–1323. <https://doi.org/10.1046/j.1365-3040.2002.00910.x>.

(12) Hirata, M.; Nakamura, K.-I.; Kondo, S. Pigment Cell Distributions in Different Tissues of the Zebrafish, with Special Reference to the Striped Pigment Pattern. *Developmental Dynamics* **2005**, *234* (2), 293–300. <https://doi.org/10.1002/dvdy.20513>.

(13) Shawkey, M. D.; D’Alba, L. Interactions between Colour-Producing Mechanisms and Their Effects on the Integumentary Colour Palette. *Philos Trans R Soc Lond B Biol Sci* **2017**, *372* (1724), 20160536. <https://doi.org/10.1098/rstb.2016.0536>.

(14) Escribano-Bailón, T.; Álvarez-García, M.; Rivas-Gonzalo, J. C.; Heredia, F. J.; Santos-Buelga, C. Color and Stability of Pigments Derived from the Acetaldehyde-Mediated Condensation between Malvidin 3-O-Glucoside and (+)-Catechin. *J. Agric. Food Chem.* **2001**, *49* (3), 1213–1217. <https://doi.org/10.1021/jf001081l>.

(15) Timberlake, C. F.; Bridle, P. Interactions Between Anthocyanins, Phenolic Compounds, and Acetaldehyde and Their Significance in Red Wines. *Am J Enol Vitic.* **1976**, *27* (3), 97–105. <https://doi.org/10.5344/ajev.1976.27.3.97>.

(16) Meléndez-Martínez, A. J.; Vicario, I. M.; Heredia, F. J. [Stability of carotenoid pigments in foods]. *Arch Latinoam Nutr* **2004**, *54* (2), 209–215.

(17) Harsito, C.; Prabowo, A. R.; Prasetyo, S. D.; Arifin, Z. Enhancement Stability and Color Fastness of Natural Dye: A Review. *Open Engineering* **2021**, *11* (1), 548–555. <https://doi.org/10.1515/eng-2021-0055>.

(18) Haddock, S. H. D.; Moline, M. A.; Case, J. F. Bioluminescence in the Sea. *Annual Review of Marine Science* **2010**, *2* (1), 443–493. <https://doi.org/10.1146/annurev-marine-120308-081028>.

(19) Wilson, T.; Hastings, J. W. Bioluminescence. *Annu Rev Cell Dev Biol* **1998**, *14*, 197–230. <https://doi.org/10.1146/annurev.cellbio.14.1.197>.

(20) Murthy, K. V. R.; Virk, H. S. Luminescence Phenomena: An Introduction. *DDF* **2013**, *347*, 1–34. <https://doi.org/10.4028/www.scientific.net/DDF.347.1>.

(21) Hooke, R. *Micrographia: Or, Some Physiological Descriptions of Minute Bodies Made by Magnifying Glasses. With Observations and Inquiries Thereupon.*, 1st ed.; J. Martyn and J. Allestry: London, England, 1665.

(22) Newton, I. *Opticks, Or, A Treatise of the Reflections, Refractions, Inflections & Colours of Light*; Courier Corporation, 1952.

(23) Poulidakos, L. V.; Lawrence, M.; Barton, D. R.; Jeffrey, S. S.; Dionne, J. A. Guided-Mode-Resonant Dielectric Metasurfaces for Colorimetric Imaging of Material Anisotropy in Fibrous Biological Tissue. *ACS Photonics* **2020**, *7* (11), 3216–3227. <https://doi.org/10.1021/acsp Photonics.0c01303>.

(24) Balaur, E.; O’Toole, S.; Spurling, A. J.; Mann, G. B.; Yeo, B.; Harvey, K.; Sadatnajafi, C.; Hanssen, E.; Orian, J.; Nugent, K. A.; Parker, B. S.; Abbey, B. Colorimetric Histology Using Plasmonically Active Microscope Slides. *Nature* **2021**, *598*, 65–71. <https://doi.org/10.1038/s41586-021-03835-2>.

(25) Wang, H.; Zhang, K.-Q. Photonic Crystal Structures with Tunable Structure Color as Colorimetric Sensors. *Sensors* **2013**, *13* (4), 4192–4213. <https://doi.org/10.3390/s130404192>.

(26) Qin, M.; Sun, M.; Hua, M.; He, X. Bioinspired Structural Color Sensors Based on Responsive Soft Materials. *Current Opinion in Solid State and Materials Science* **2019**, *23* (1), 13–27. <https://doi.org/10.1016/j.cossms.2018.10.001>.

(27) Haddadin, Z.; Pike, T.; Moses, J. J.; Poulidakos, L. V. Colorimetric Metasurfaces Shed Light on Fibrous Biological Tissue. *J. Mater. Chem. C* **2021**, *9* (35), 11619–11639. <https://doi.org/10.1039/D1TC02030G>.

- (28) Cai, L.; Wang, H.; Yu, Y.; Bian, F.; Wang, Y.; Shi, K.; Ye, F.; Zhao, Y. Stomatocyte Structural Color-Barcode Micromotors for Multiplex Assays. *National Science Review* **2020**, *7* (3), 644–651. <https://doi.org/10.1093/nsr/nwz185>.
- (29) Zhang, H.; Guo, J.; Wang, Y.; Sun, L.; Zhao, Y. Stretchable and Conductive Composite Structural Color Hydrogel Films as Bionic Electronic Skins. *Advanced Science* **2021**, *8* (20), 2102156. <https://doi.org/10.1002/advs.202102156>.
- (30) Lee, J. H.; Fan, B.; Samdin, T. D.; Monteiro, D. A.; Desai, M. S.; Scheideler, O.; Jin, H.-E.; Kim, S.; Lee, S.-W. Phage-Based Structural Color Sensors and Their Pattern Recognition Sensing System. *ACS Nano* **2017**, *11* (4), 3632–3641. <https://doi.org/10.1021/acsnano.6b07942>.
- (31) Zhou, J.; Han, P.; Liu, M.; Zhou, H.; Zhang, Y.; Jiang, J.; Liu, P.; Wei, Y.; Song, Y.; Yao, X. Self-Healable Organogel Nanocomposite with Angle-Independent Structural Colors. *Angewandte Chemie* **2017**, *129* (35), 10598–10602. <https://doi.org/10.1002/ange.201705462>.
- (32) Sun, S.; Yang, W.; Zhang, C.; Jing, J.; Gao, Y.; Yu, X.; Song, Q.; Xiao, S. Real-Time Tunable Colors from Microfluidic Reconfigurable All-Dielectric Metasurfaces. *ACS Nano* **2018**, *12* (3), 2151–2159. <https://doi.org/10.1021/acsnano.7b07121>.
- (33) Olson, J.; Manjavacas, A.; Liu, L.; Chang, W.-S.; Foerster, B.; King, N. S.; Knight, M. W.; Nordlander, P.; Halas, N. J.; Link, S. Vivid, Full-Color Aluminum Plasmonic Pixels. *Proceedings of the National Academy of Sciences* **2014**, *111* (40), 14348–14353. <https://doi.org/10.1073/pnas.1415970111>.
- (34) Olson, J.; Manjavacas, A.; Basu, T.; Huang, D.; Schlather, A. E.; Zheng, B.; Halas, N. J.; Nordlander, P.; Link, S. High Chromaticity Aluminum Plasmonic Pixels for Active Liquid Crystal Displays. *ACS Nano* **2016**, *10* (1), 1108–1117. <https://doi.org/10.1021/acsnano.5b06415>.
- (35) Zhang, W.; Anaya, M.; Lozano, G.; Calvo, M. E.; Johnston, M. B.; Míguez, H.; Snaith, H. J. Highly Efficient Perovskite Solar Cells with Tunable Structural Color. *Nano Lett.* **2015**, *15* (3), 1698–1702. <https://doi.org/10.1021/nl504349z>.
- (36) Zhou, H.; Xu, J.; Liu, X.; Zhang, H.; Wang, D.; Chen, Z.; Zhang, D.; Fan, T. Bio-Inspired Photonic Materials: Prototypes and Structural Effect Designs for Applications in Solar Energy Manipulation. *Advanced Functional Materials* **2018**, *28* (24), 1705309. <https://doi.org/10.1002/adfm.201705309>.
- (37) Li, Z.; Li, S.; Ma, T. Using Photonic Glasses as Colored Covers for Solar Energy Harvesting. *Advanced Optical Materials* **2013**, *11* (5), 2202370. <https://doi.org/10.1002/adom.202202370>.
- (38) Shang, L.; Zhang, W.; Xu, K.; Zhao, Y. Bio-Inspired Intelligent Structural Color Materials. *Materials Horizons* **2019**, *6* (5), 945–958. <https://doi.org/10.1039/C9MH00101H>.
- (39) Goh, X. M.; Zheng, Y.; Tan, S. J.; Zhang, L.; Kumar, K.; Qiu, C.-W.; Yang, J. K. W. Three-Dimensional Plasmonic Stereoscopic Prints in Full Colour. *Nat Commun* **2014**, *5* (1), 5361. <https://doi.org/10.1038/ncomms6361>.
- (40) Yang, W.; Xiao, S.; Song, Q.; Liu, Y.; Wu, Y.; Wang, S.; Yu, J.; Han, J.; Tsai, D.-P. All-Dielectric Metasurface for High-Performance Structural Color. *Nat Commun* **2020**, *11* (1), 1864. <https://doi.org/10.1038/s41467-020-15773-0>.
- (41) Kumar, K.; Duan, H.; Hegde, R. S.; Koh, S. C. W.; Wei, J. N.; Yang, J. K. W. Printing Colour at the Optical Diffraction Limit. *Nat Nanotechnol* **2012**, *7* (9), 557–561. <https://doi.org/10.1038/nnano.2012.128>.
- (42) Jeong, H.; Yang, Y.; Cho, H.; Badloe, T.; Kim, I.; Ma, R.-M.; Rho, J. Emerging Advanced Metasurfaces: Alternatives to Conventional Bulk Optical Devices. *Microelectronic Engineering* **2020**, *220*, 111146. <https://doi.org/10.1016/j.mee.2019.111146>.
- (43) Yang, B.; Liu, W.; Li, Z.; Cheng, H.; Chen, S.; Tian, J. Polarization-Sensitive Structural Colors with Hue-and-Saturation Tuning Based on All-Dielectric Nanopixels. *Advanced Optical Materials* **2018**, *6* (4), 1701009. <https://doi.org/10.1002/adom.201701009>.
- (44) Lawrence, M.; Barton, D. R.; Dixon, J.; Song, J.-H.; van de Groep, J.; Brongersma, M. L.; Dionne, J. A. High Quality Factor Phase Gradient Metasurfaces. *Nat. Nanotechnol.* **2020**, *15* (11), 956–961. <https://doi.org/10.1038/s41565-020-0754-x>.
- (45) Ellenbogen, T.; Seo, K.; Crozier, K. B. Chromatic Plasmonic Polarizers for Active Visible Color Filtering and Polarimetry. *Nano Lett.* **2012**, *12* (2), 1026–1031. <https://doi.org/10.1021/nl204257g>.
- (46) Kristensen, A.; Yang, J. K. W.; Bozhevolnyi, S. I.; Link, S.; Nordlander, P.; Halas, N. J.; Mortensen, N. A. Plasmonic Colour Generation. *Nat Rev Mater* **2016**, *2*, 16088. <https://doi.org/10.1038/natrevmats.2016.88>.
- (47) Yang, J.-H.; Babicheva, V. E.; Yu, M.-W.; Lu, T.-C.; Lin, T.-R.; Chen, K.-P. Structural Colors Enabled by Lattice Resonance on Silicon Nitride Metasurfaces. *ACS Nano* **2020**, *14* (5), 5678–5685. <https://doi.org/10.1021/acsnano.0c00185>.
- (48) Park, C.-S.; Koirala, I.; Gao, S.; Shrestha, V. R.; Lee, S.-S.; Choi, D.-Y. Structural Color Filters Based on an All-Dielectric Metasurface Exploiting Silicon-Rich Silicon Nitride Nanodisks. *Opt. Express, OE* **2019**, *27* (2), 667–679. <https://doi.org/10.1364/OE.27.000667>.
- (49) Proust, J.; Bedu, F.; Gallas, B.; Ozerov, I.; Bonod, N. All-Dielectric Colored Metasurfaces with Silicon Mie Resonators. *ACS Nano* **2016**, *10* (8), 7761–7767. <https://doi.org/10.1021/acsnano.6b03207>.
- (50) Vashistha, V.; Vaidya, G.; Hegde, R. S.; Serebryannikov, A. E.; Bonod, N.; Krawczyk, M. All-Dielectric Metasurfaces Based on Cross-Shaped Resonators for Color Pixels with Extended Gamut. *ACS Photonics* **2017**, *4* (5), 1076–1082. <https://doi.org/10.1021/acsp Photonics.6b00853>.
- (51) Wu, L.; Cheng, K.; Lin, Y.-S. All-Dielectric Nanostructured Metasurfaces with Ultrahigh Color Purity and Selectivity for Refractive Index Sensing Applications. *Results in Physics* **2022**, *43*, 106092. <https://doi.org/10.1016/j.rinp.2022.106092>.
- (52) Lin, L.; Wang, M.; Wei, X.; Peng, X.; Xie, C.; Zheng, Y. Photoswitchable Rabi Splitting in Hybrid Plasmon-Waveguide Modes. *Nano Lett.* **2016**, *16* (12), 7655–7663. <https://doi.org/10.1021/acs.nanolett.6b03702>.
- (53) Dănilă, O. Spectroscopic Assessment of a Simple Hybrid Si-Au Cell Metasurface-Based Sensor in the Mid-Infrared Domain. *Journal of Quantitative Spectroscopy and Radiative Transfer* **2020**, *254*, 107209. <https://doi.org/10.1016/j.jqsrt.2020.107209>.
- (54) Kang, E. S. H.; Shiran Chaharsoughi, M.; Rossi, S.; Jonsen, M. P. Hybrid Plasmonic Metasurfaces. *Journal of Applied Physics* **2019**, *126* (14), 140901. <https://doi.org/10.1063/1.5116885>.
- (55) Caligiuri, V.; Patra, A.; De Santo, M. P.; Forestiero, A.; Papuzzo, G.; Aceti, D. M.; Lio, G. E.; Barberi, R.; De Luca, A. Hybrid Plasmonic/Photonic Nanoscale Strategy for Multilevel Anticounterfeit Labels. *ACS Appl. Mater. Interfaces* **2021**, *13* (41), 49172–49183. <https://doi.org/10.1021/acsaami.1c13701>.
- (56) Jung, Y.; Jung, H.; Choi, H.; Lee, H. Polarization Selective Color Filter Based on Plasmonic Nanograting Embedded Etalon Structures. *Nano Lett.* **2020**, *20* (9), 6344–6350. <https://doi.org/10.1021/acs.nanolett.0c01738>.
- (57) Kim, Y.; Jung, K.; Cho, J.; Hyun, J. K. Realizing Vibrant and High-Contrast Reflective Structural Colors from Lossy Metals Supporting Dielectric Gratings. *ACS Nano* **2019**, *13* (9), 10717–10726. <https://doi.org/10.1021/acsnano.9b05382>.
- (58) Xu, T.; Wu, Y.-K.; Luo, X.; Guo, L. J. Plasmonic Nanoresonators for High-Resolution Colour Filtering and Spectral Imaging. *Nat Commun* **2010**, *1*, 59. <https://doi.org/10.1038/ncomms1058>.
- (59) Lee, Y.; Park, M.-K.; Kim, S.; Shin, J. H.; Moon, C.; Hwang, J. Y.; Choi, J.-C.; Park, H.; Kim, H.-R.; Jang, J. E. Electrical Broad Tuning of Plasmonic Color Filter Employing an Asymmetric-Lattice Nanohole Array of Metasurface Controlled by Polarization Rotator. *ACS Photonics* **2017**, *4* (8), 1954–1966. <https://doi.org/10.1021/acsp Photonics.7b00249>.
- (60) Sharma, M.; Hendler, N.; Ellenbogen, T. Electrically Switchable Color Tags Based on Active Liquid-Crystal Plasmonic

- Metasurface Platform. *Advanced Optical Materials* **2020**, *8* (7), 1901182. <https://doi.org/10.1002/adom.201901182>.
- (61) Khurgin, J. B.; Sun, G. In Search of the Elusive Lossless Metal. *Applied Physics Letters* **2010**, *96* (18), 181102. <https://doi.org/10.1063/1.3425890>.
- (62) Raman, A.; Shin, W.; Fan, S. Upper Bound on the Modal Material Loss Rate in Plasmonic and Metamaterial Systems. *Phys. Rev. Lett.* **2013**, *110* (18), 183901. <https://doi.org/10.1103/PhysRevLett.110.183901>.
- (63) Miller, O. D.; Polimeridis, A. G.; Reid, M. T. H.; Hsu, C. W.; DeLacy, B. G.; Joannopoulos, J. D.; Soljačić, M.; Johnson, S. G. Fundamental Limits to Optical Response in Absorptive Systems. *Opt. Express, OE* **2016**, *24* (4), 3329–3364. <https://doi.org/10.1364/OE.24.003329>.
- (64) Uddin, M. J.; Khaleque, T.; Magnusson, R. Guided-Mode Resonant Polarization-Controlled Tunable Color Filters. *Opt. Express, OE* **2014**, *22* (10), 12307–12315. <https://doi.org/10.1364/OE.22.012307>.
- (65) Uddin, M. J.; Magnusson, R. Highly Efficient Color Filter Array Using Resonant Si₃N₄ Gratings. *Opt. Express, OE* **2013**, *21* (10), 12495–12506. <https://doi.org/10.1364/OE.21.012495>.
- (66) Tseng, M. L.; Jahani, Y.; Leitis, A.; Altug, H. Dielectric Metasurfaces Enabling Advanced Optical Biosensors. *ACS Photonics* **2021**, *8* (1), 47–60. <https://doi.org/10.1021/acsphotonics.0c01030>.
- (67) Evlyukhin, A. B.; Novikov, S. M.; Zyviets, U.; Eriksen, R. L.; Reinhardt, C.; Bozhevolnyi, S. I.; Chichkov, B. N. Demonstration of Magnetic Dipole Resonances of Dielectric Nanospheres in the Visible Region. *Nano Lett.* **2012**, *12* (7), 3749–3755. <https://doi.org/10.1021/nl301594s>.
- (68) Kuznetsov, A. I.; Miroshnichenko, A. E.; Fu, Y. H.; Zhang, J.; Luk'yanchuk, B. Magnetic Light. *Sci Rep* **2012**, *2* (1), 492. <https://doi.org/10.1038/srep00492>.
- (69) Kivshar, Y.; Miroshnichenko, A. Meta-Optics with Mie Resonances. *Optics & Photonics News, OPN* **2017**, *28* (1), 24–31. <https://doi.org/10.1364/OPN.28.1.000024>.
- (70) Tzarouchis, D.; Sihvola, A. Light Scattering by a Dielectric Sphere: Perspectives on the Mie Resonances. *Applied Sciences* **2018**, *8* (2), 184. <https://doi.org/10.3390/app8020184>.
- (71) Baek, K.; Kim, Y.; Mohd-Noor, S.; Hyun, J. K. Mie Resonant Structural Colors. *ACS Appl Mater Interfaces* **2020**, *12* (5), 5300–5318. <https://doi.org/10.1021/acsami.9b16683>.
- (72) Wang, B.; Xu, Y.; Wu, Z.; Zhang, Z.; Wang, Q. All-Dielectric Metasurface-Based Color Filter in CMOS Image Sensor. *Optics Communications* **2023**, *540*, 129485. <https://doi.org/10.1016/j.optcom.2023.129485>.
- (73) Vashistha, V.; Vaidya, G.; Gruszecki, P.; Serebryannikov, A. E.; Krawczyk, M. Polarization Tunable All-Dielectric Color Filters Based on Cross-Shaped Si Nanoantennas. *Sci Rep* **2017**, *7* (1), 8092. <https://doi.org/10.1038/s41598-017-07986-z>.
- (74) Zhou, Y.; Wang, B.; Guo, Z.; Wu, X. Guided Mode Resonance Sensors with Optimized Figure of Merit. *Nanomaterials* **2019**, *9* (6), 837. <https://doi.org/10.3390/nano9060837>.
- (75) Højlund-Nielsen, E.; Weirich, J.; Nørregaard, J.; Garnæs, J.; Mortensen, N. A.; Kristensen, A. Angle-Independent Structural Colors of Silicon. *JNP* **2014**, *8* (1), 083988. <https://doi.org/10.1117/1.JNP.8.083988>.
- (76) Shen, S.; Ruan, Z.; Li, S.; Yuan, Y.; Tan, H. The Influence of Periodicity on the Optical Response of Cube Silicon Metasurfaces. *Results in Physics* **2021**, *23*, 104057. <https://doi.org/10.1016/j.rinp.2021.104057>.
- (77) Babicheva, V. E.; Evlyukhin, A. B. Multipole Lattice Effects in High Refractive Index Metasurfaces. *Journal of Applied Physics* **2021**, *129* (4), 040902. <https://doi.org/10.1063/5.0024274>.
- (78) Zakomirnyi, V. I.; Ershov, A. E.; Gerasimov, V. S.; Karpov, S. V.; Ågren, H.; Rasskazov, I. L. Collective Lattice Resonances in Arrays of Dielectric Nanoparticles: A Matter of Size. *Opt. Lett., OL* **2019**, *44* (23), 5743–5746. <https://doi.org/10.1364/OL.44.005743>.
- (79) Zakomirnyi, V. I.; Karpov, S. V.; Ågren, H.; Rasskazov, I. L. Collective Lattice Resonances in Disordered and Quasi-Random All-Dielectric Metasurfaces. *J. Opt. Soc. Am. B, JOSAB* **2019**, *36* (7), E21–E29. <https://doi.org/10.1364/JOSAB.36.000E21>.
- (80) Castellanos, G. W.; Bai, P.; Gómez Rivas, J. Lattice Resonances in Dielectric Metasurfaces. *Journal of Applied Physics* **2019**, *125* (21), 213105. <https://doi.org/10.1063/1.5094122>.
- (81) Babicheva, V. E.; Evlyukhin, A. B. Analytical Model of Resonant Electromagnetic Dipole-Quadrupole Coupling in Nanoparticle Arrays. *Phys. Rev. B* **2019**, *99* (19), 195444. <https://doi.org/10.1103/PhysRevB.99.195444>.
- (82) Babicheva, V. E. Lattice Effect in Mie-Resonant Dielectric Nanoparticle Array under Oblique Light Incidence. *MRS Communications* **2018**, *8* (4), 1455–1462. <https://doi.org/10.1557/mrc.2018.216>.
- (83) Babicheva, V. E.; Evlyukhin, A. B. Interplay and Coupling of Electric and Magnetic Multipole Resonances in Plasmonic Nanoparticle Lattices. *MRS Communications* **2018**, *8* (3), 712–717. <https://doi.org/10.1557/mrc.2018.112>.
- (84) Babicheva, V. E.; Evlyukhin, A. B. Nanoparticle Lattices with Electric and Magnetic Resonances [Prospective]. *MRS Communications* **2018**, *8* (3), 712–717. <https://doi.org/10.1557/mrc.2018.112>.
- (85) Babicheva, V. E.; Evlyukhin, A. B. Metasurfaces with Electric Quadrupole and Magnetic Dipole Resonant Coupling. *ACS Photonics* **2018**, *5* (5), 2022–2033. <https://doi.org/10.1021/acsphotonics.7b01520>.
- (86) Babicheva, V. E.; Evlyukhin, A. B. Resonant Lattice Kerker Effect in Metasurfaces With Electric and Magnetic Optical Responses. *Laser & Photonics Reviews* **2017**, *11* (6), 1700132. <https://doi.org/10.1002/lpor.201700132>.
- (87) Smith, T.; Guild, J. The C.I.E. Colorimetric Standards and Their Use. *Trans. Opt. Soc.* **1931**, *33* (3), 73. <https://doi.org/10.1088/1475-4878/33/3/301>.
- (88) Sharma, G. *Digital Color Imaging Handbook*; 2003.
- (89) COMSOL Multiphysics® v5.6, 2020. www.comsol.com.
- (90) Wave Optics Module User's Guide., 2020. <https://doc.comsol.com/5.6/doc/com.comsol.help.waveoptics/WaveOpticsModuleUsersGuide.pdf> (accessed 2023-06-05).
- (91) San Diego Supercomputer Center. Triton Shared Computer Cluster, 2023. <https://doi.org/10.57873/T34W2R>.
- (92) 8.2.1 CIE 1976 (L*a*b*) Colour Space; CIELAB Colour Space. In *Colorimetry*; Internationale Beleuchtungskommission, Ed.; CIE; Comm. Internat. de l'éclairage: Wien, 2004; pp 17–18.
- (93) Fairchild, M. D. 10.3 CIELAB. In *Color Appearance Models*; John Wiley & Sons: England, 2005; p 185.
- (94) Fairchild, M. D. 4.6 Saturation. In *Color Appearance Models*; John Wiley & Sons: England, 2005; p 88.
- (95) Schiller, F.; Gegenfurtner, K. R. Perception of Saturation in Natural Scenes. *J. Opt. Soc. Am. A, JOSAA* **2016**, *33* (3), A194–A206. <https://doi.org/10.1364/JOSAA.33.00A194>.
- (96) Schiller, F.; Valsecchi, M.; Gegenfurtner, K. R. An Evaluation of Different Measures of Color Saturation. *Vision Research* **2018**, *151*, 117–134. <https://doi.org/10.1016/j.visres.2017.04.012>.
- (97) Hedjar, L.; Toscani, M.; Gegenfurtner, K. R. Perception of Saturation in Natural Objects. *J. Opt. Soc. Am. A, JOSAA* **2023**, *40* (3), A190–A198. <https://doi.org/10.1364/JOSAA.476874>.
- (98) Greenfield, N. J. Using Circular Dichroism Spectra to Estimate Protein Secondary Structure. *Nat Protoc* **2006**, *1* (6), 2876–2890. <https://doi.org/10.1038/nprot.2006.202>.

Cutting corners to suppress high-order modes in Mie resonator arrays*Supplementary Material*

Authors: Zaid Haddadin¹, Shahrose Khan², Lisa V. Poulikakos^{*,2,3}

¹Department of Electrical & Computer Engineering, UC San Diego

²Department of Mechanical & Aerospace Engineering, UC San Diego

³Materials Science & Engineering Program, UC San Diego

Keywords: lattice, resonances, metasurfaces, saturation, silicon nitride, structural colour

Table of Contents

Table of Contents	1
Section S1: COMSOL Multiphysics® v5.6 Set Up	2
S1.1: Global Definitions	2
S1.2: Component 1	4
Section S2: Predicting structural colour outputs	14
Section S3: Evaluating colour saturation	17
Section S3.1: Calculating L*a*b* values	17
Section S4: Rectangle-shaped nanostructure arrays	18
Section S5: Rectangle-bound t-shaped nanostructure arrays	19
Section S6: Square-bound t-shaped nanostructure arrays	21
Section S6.1: Square-shaped nanostructure arrays	21
Section S6.2: Cutting corners of square-shaped nanostructures	22
Section S6.4: Saturation scores of square-bound nanostructure arrays	25
Section S6.5: Orthogonal polarisations reflectance spectra	26
Section S7: Programming Scripts	28
Section S7.1: Python	28
Section S7.2: Mathematica	31
Section S8: Data	33
Section S8.1: Square-shaped nanostructure arrays	33
Section S8.2: Rectangle-shaped nanostructure arrays	33
Section S8.3: Rectangle-bound t-shaped nanostructure arrays	34
Section S8.4: Square-bound t-shaped nanostructure arrays	35
References	37

Section S1: COMSOL Multiphysics® v5.6 Set Up

The COMSOL Multiphysics® v5.6 base software [1] and the Wave Optics Module [2] were used to for this study. The COMSOL Multiphysics® file was created with an “Electromagnetic Waves, Frequency Domain” layer in the three-dimensional (3D) space. The file is created with an empty study.

S1.1: Global Definitions

Three sub-layers were created underneath the default “Global Definitions” layer: (i) “Nanostructure Parameters”, (ii) “Model Parameters”, and (iii) “Optics Parameters”. The attributes and entries contained in these layers can be seen in Tables S1-S3

Table S1. “Nanostructure Parameters” attributes and entries. “Dep. Var.” entries in the “Expression” and “Value” columns denote dependent variables that changed among simulations. By altering the *_depth and *_width attribute entries, it’s possible to create square-, rectangle-, and t-shaped nanoparticles. (* = wildcard: any character or sequence of characters)

Name	Expression	Value	Description
A_interresonator_gap	100 [nm]	1E-7 m	The distance between nanostructure A and an adjacent one.
A_nanostructure_depth	<i>Dep. Var.</i>	<i>Dep. Var.</i>	The depth of nanostructure A.
A_nanostructure_width	<i>Dep. Var.</i>	<i>Dep. Var.</i>	The width of nanostructure A.
B_interresonator_gap	100 [nm]	1E-7 m	The distance between nanostructure B and an adjacent one.
B_nanostructure_depth	<i>Dep. Var.</i>	<i>Dep. Var.</i>	The depth of nanostructure B.
B_nanostructure_width	<i>Dep. Var.</i>	<i>Dep. Var.</i>	The width of nanostructure B.
nanostructure_thickness	270 [nm]	2.7E-7 m	The thickness (or height) of the nanostructure.

Table S2. “Model Parameters” attributes and entries. “Indep. Var.” entries in the “Value” columns denote independent variables that changed among simulations.

Name	Expression	Value	Description
domain_depth	lattice_depth_period	4.274E-7 m	The depth of the entire domain.
domain_height	incident_height + transmitted_height + nanostructure_thickness	4.27E-6 m	The height of the entire domain. This is composed of all parts of the model.
domain_width	lattice_width_period	4.274E-7 m	The width of the entire domain.
incident_height	2000 [nm]	2E-6 m	The height of the domain through which light is incident towards the thin film.
lattice_depth_period	B_nanostructure_depth + B_interresonator_gap	<i>Indep. Var.</i>	The interval of distance between successive repetitions of the nanoresonator along the depth of the nanostructure.
lattice_width_period	A_nanostructure_width + A_interresonator_gap	<i>Indep. Var.</i>	The interval of distance between successive repetitions of the nanoresonator along the width of the nanostructure.
transmitted_height	2000 [nm]	2E-6 m	The height of the domain through which light is transmitted after passing through the thin film.

Table S3. “Optics Parameters” attributes and entries. “Dep. Var.” entries in the “Expression” and “Value” columns denote dependent variables that changed among simulations. By altering the angle_polarisation_* attribute entries, it’s possible to become alter the angle of incident polarisation. (* = wildcard: any character or sequence of characters)

Name	Expression	Value	Description
wavelength_step	1 [nm]	1E-9 m	The steps taken in incrementing/decrementing the wavelength when running the simulation.
wavelength_min	400 [nm]	4E-7 m	The minimum value the wavelength of light can take for this study.
wavelength_max	700 [nm]	7E-7 m	The maximum value the wavelength of light can take for this study.
angle_polarisation_y	Dep. Var.	Dep. Var.	The angle of the incident y-component of the polarised light.
angle_polarisation_x	Dep. Var.	Dep. Var.	The angle of the incident x-component of the polarised light.

S1.2: Component 1

S1.2.1: Definitions

In the “Definitions” layer of “Component 1”, a sub-layer is created: “Electric mode field amplitudes”. Table S4 contains the attributes and entries of this sub-layer.

Table S4. “Electric mode field amplitudes” attributes and entries.

Name	Expression	Unit	Description
Eox	- sin(angle_polarisation_x)		The x-component of the electric field amplitude.
Eoy	cos(angle_polarisation_y)		The y-component of the electric field amplitude.

S1.2.2: Geometry 1

In the “Geometry 1” layer of “Component 1” four sub-layers are added: (i) “Block” layer renamed to “Domain”; (ii) “Work Plane” layer renamed to “Nanostructure Work Plane”; (iii) “Extrude” layer; and (iv) “Form Union” layer.

(i) The settings for “Domain” layer can be seen in Figures S1.

(ii) The settings for “Nanostructure Work Plane” layer can be seen in Figure S2. Moreover, the “Nanostructure Work Plane” by default is made with a “Plane Geometry” sub-layer. Under the “Plane Geometry” sub-layer, three more layers are made: (a) “Rectangle” layer renamed to “Rectangle A” (settings in Figure S3, Left); (b) “Rectangle” layer renamed to “Rectangle B” (settings in Figure S3, Right); and (c) “Union” layer renamed to “Cross Nanostructure” (settings in Figure S4).

(iii) The settings for “Extrude” layer can be seen in Figure S5.

(iv) The settings for “Form Union” layer were set to “Form a union” for “Action:” and “Automatic” for “Repair tolerance:”.

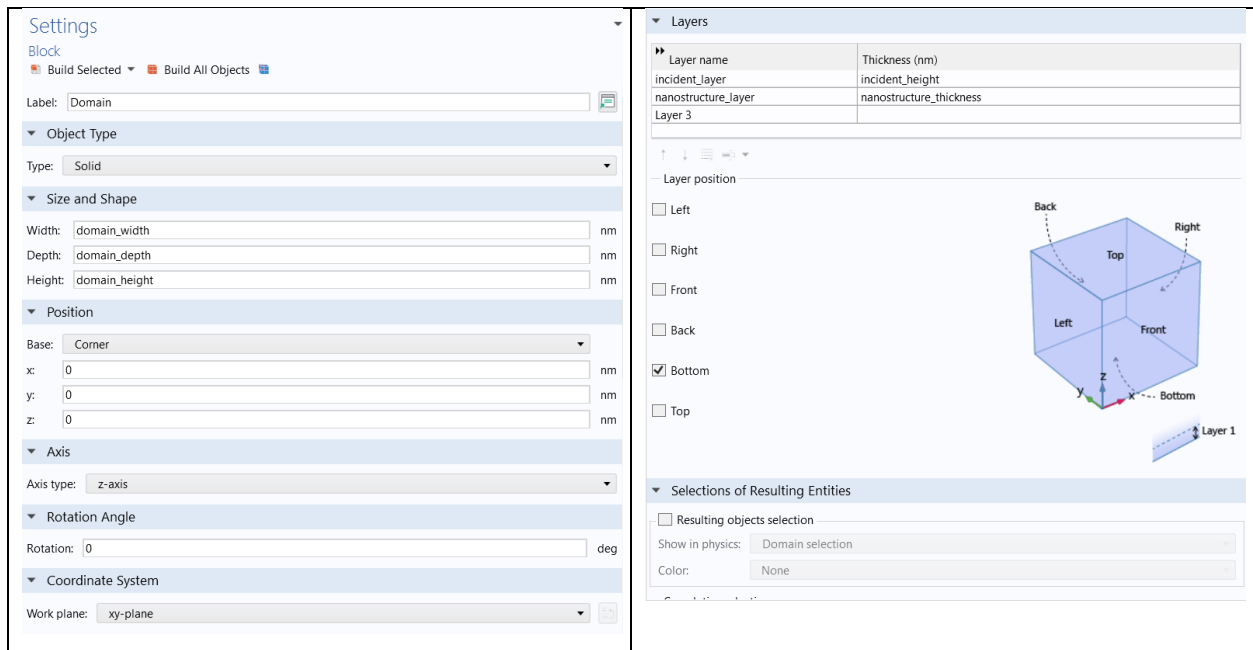


Figure S1. The settings used for the “Domain” sublayer of “Geometry 1”.

Settings

Work Plane

Build Selected Build All Objects

Label: Nanostructure Work Plane

Plane Definition

Plane type: Quick

Plane: xy-plane

Offset type: Distance

z-coordinate: incident_height nm

Local Coordinate System

Unite Objects

☒ Unite objects

Repair tolerance: Automatic

Selections of Resulting Entities

☐ Resulting objects selection

Show in physics: Boundary selection

Color: None

— Selections from plane geometry

☐ Show in physics

— Cumulative selection

Contribute to: None

New

Figure S2. The settings used for the “Nanostructure Work Plane” sublayer of “Geometry 1”.

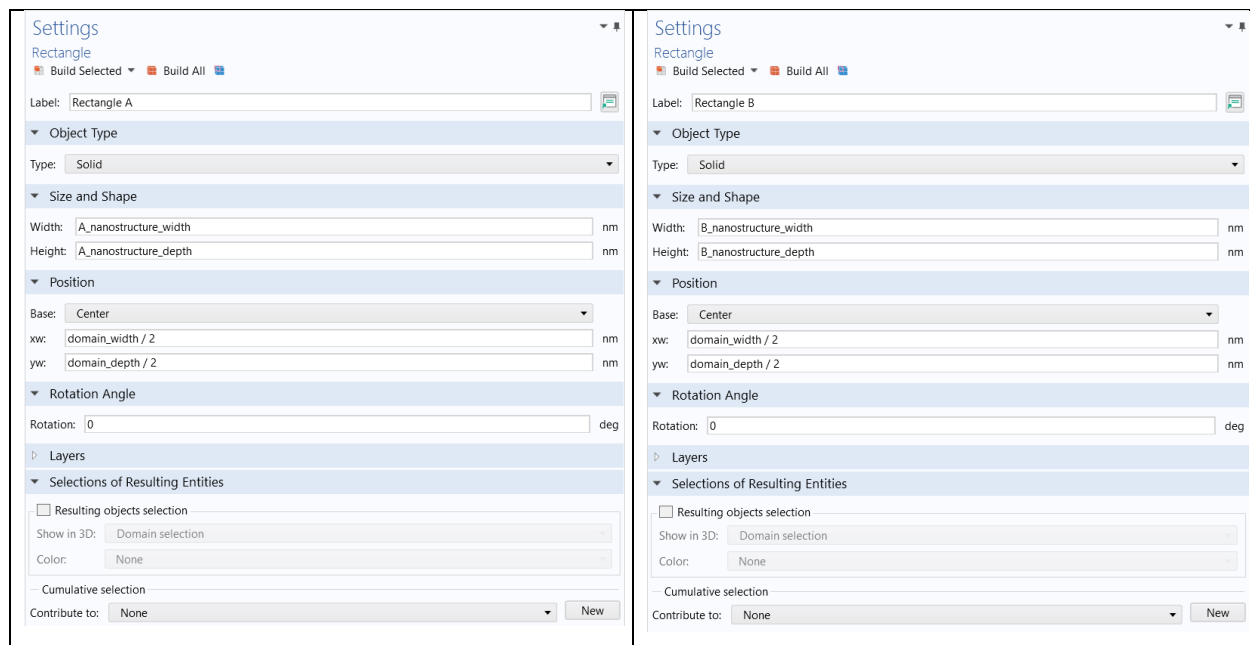


Figure S3. The settings used for **(Left)** “Rectangle A” and **(Right)** “Rectangle B” sub-layers of “Nanostructure Work Plane”.

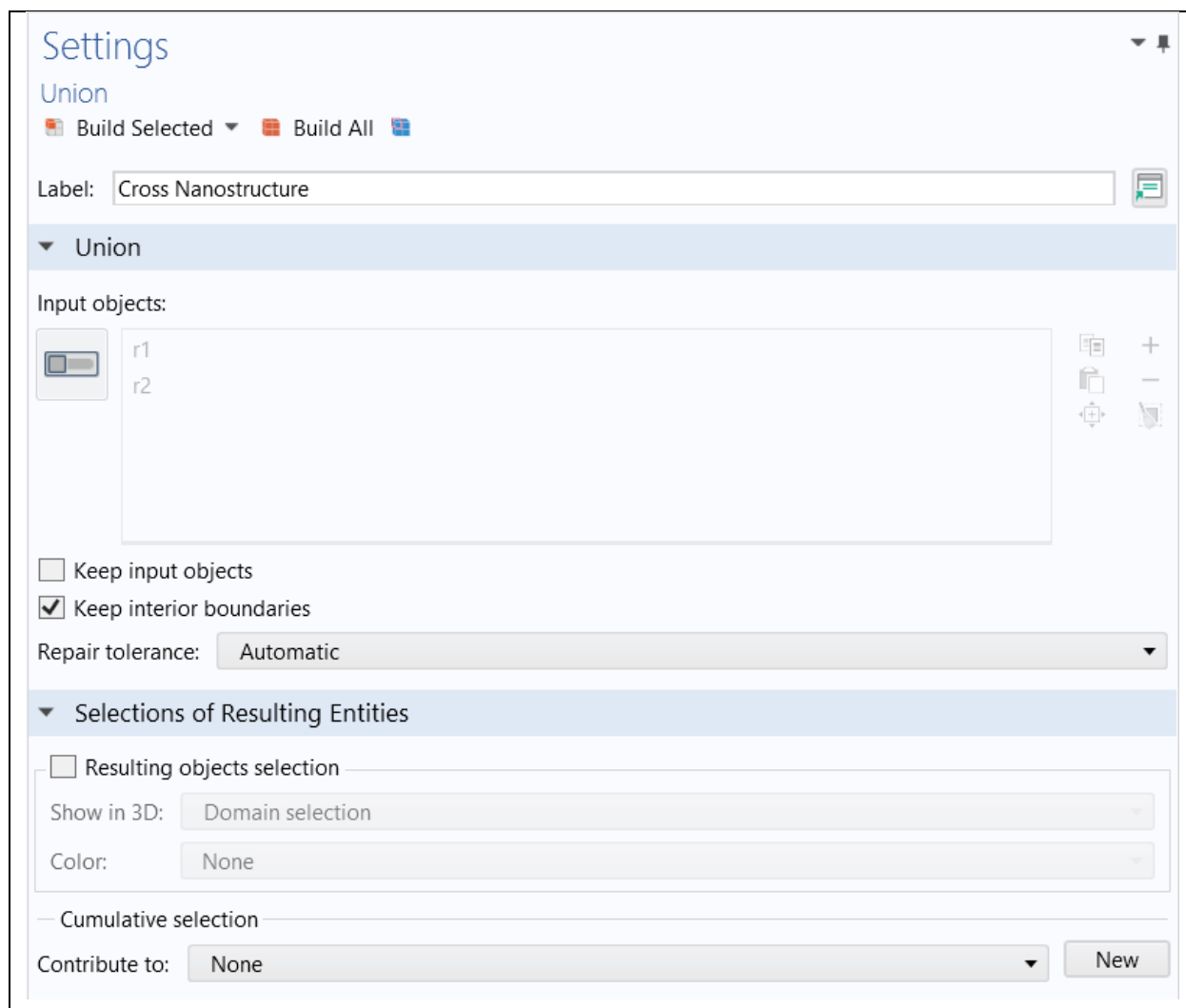


Figure S4. The settings used for the “Cross Nanostructure” sub-layer of “Nanostructure Work Plane”. The “r1” and “r2” objects in the settings refer to the “Rectangle A” and “Rectangle B” sub-layers, respectively.

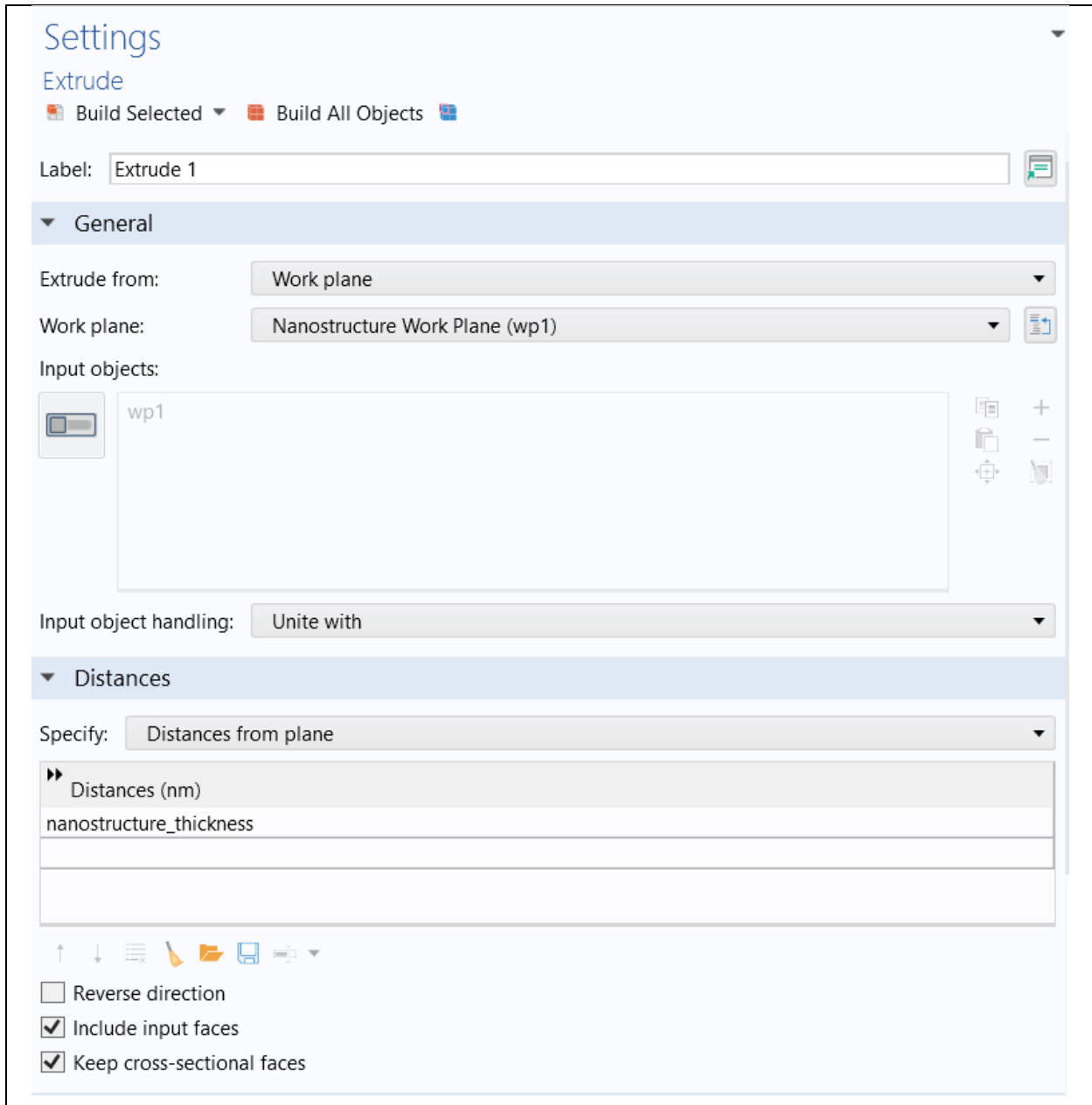


Figure S5. The settings used for the “Extrude” layer of “Geometry 1”. The “wp1” object in the settings refer to the “Nanostructure Work Plane” layer.

S1.2.3: Materials

Three materials were added using the in-built COMSOL Multiphysics® v5.6 Wave Optics Module library: (i) “Air (Ciddor 1996: n 0.23-1.690 μm)” [3]; (ii) “Si₃N₄ (Silicon nitride) (Luke et al. 2015: n 0.310-5.504 μm)” [4]; and (iii) “SiO₂ (Silicon dioxide, Silica, Quartz) (Ghosh 1999: \hat{n} ±-Quartz, $n(o)$ 0.198-2.0531 μm)” [5]. Figure S6 shows the distribution of the materials in the model.

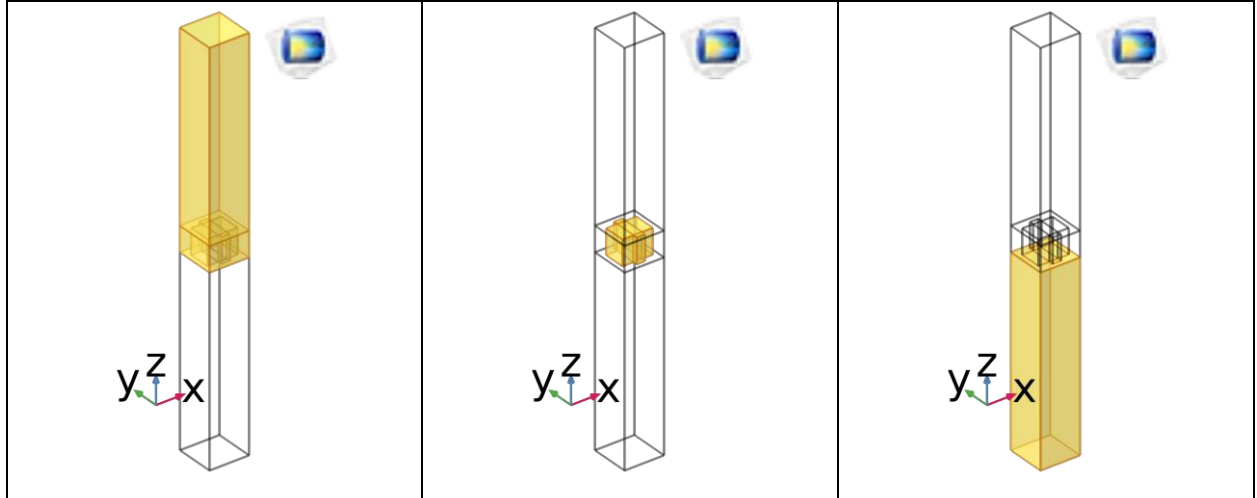


Figure S6. The yellow highlights represent the distribution of **(Left)** air, **(Middle)** silicon nitride, and **(Right)** silicon dioxide in the model. Air encompasses domains 2-3. Silicon nitride encompasses domains 4-8. Silicon dioxide encompasses domain 1. Images provided using the COMSOL Multiphysics® in-built functionality.

S1.2.4: Electromagnetic Waves, Frequency Domain

The “Formulation” of the “Electromagnetic Waves, Frequency Domain” layer is set to “Full field”. By default, three sub-layers are provided with this layer: (i) “Wave Equation, Electric 1”; (ii) “Perfect Electric Conductor 1”; and (iii) “Initial Values 1”. Figure S7 shows the settings of “Wave Equation, Electric 1” and “Initial Values”. “Perfect Electric Conductor 1” is overridden by future settings; thus, the settings are not provided in this write-up.

Moreover, four additional sub-layers are created: (iv) “Port” layer named “Port 1”; (v) “Port” layer named “Port 2”; (vi) “Periodic Condition” layer named “Periodic Condition 1”; (vii) “Periodic Condition” layer named “Periodic Condition 2”.

(iv) “Port 1” layer settings are provided in Figure S8. The “Add Diffraction Orders” at the bottom of the settings was selected. This added a “Orthogonal Polarization 1” layer under “Port 1” and under “Port 2”, and sixteen “Diffraction Order” layers under “Port 2”.

(v) “Port 2” layer settings are provided in Figure S9.

(vi) “Periodic Condition 1” layer settings are provided in Figure S10, Left.

(vii) “Periodic Condition 2” layer settings are provided in Figure S10, Right.

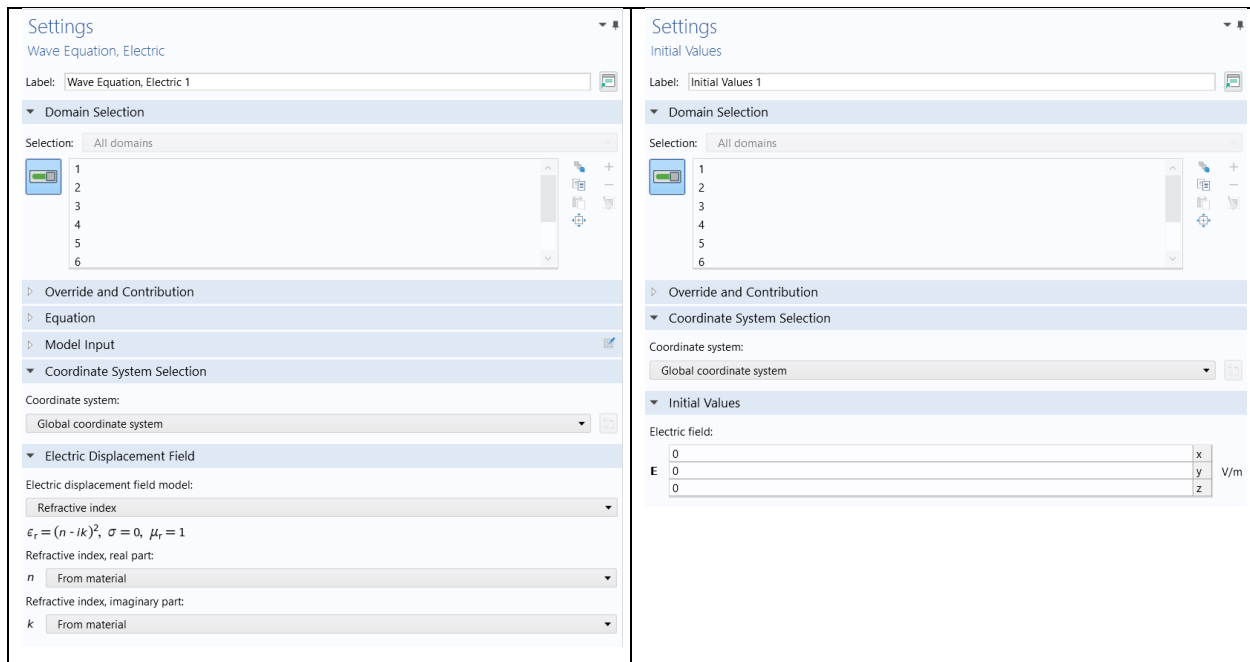


Figure S7. Settings for the (*Left*) “Wave Equation, Electric 1” layer and (*Right*) “Initial Values 1” layer of the parent “Electromagnetic Waves, Frequency Domain” layer.

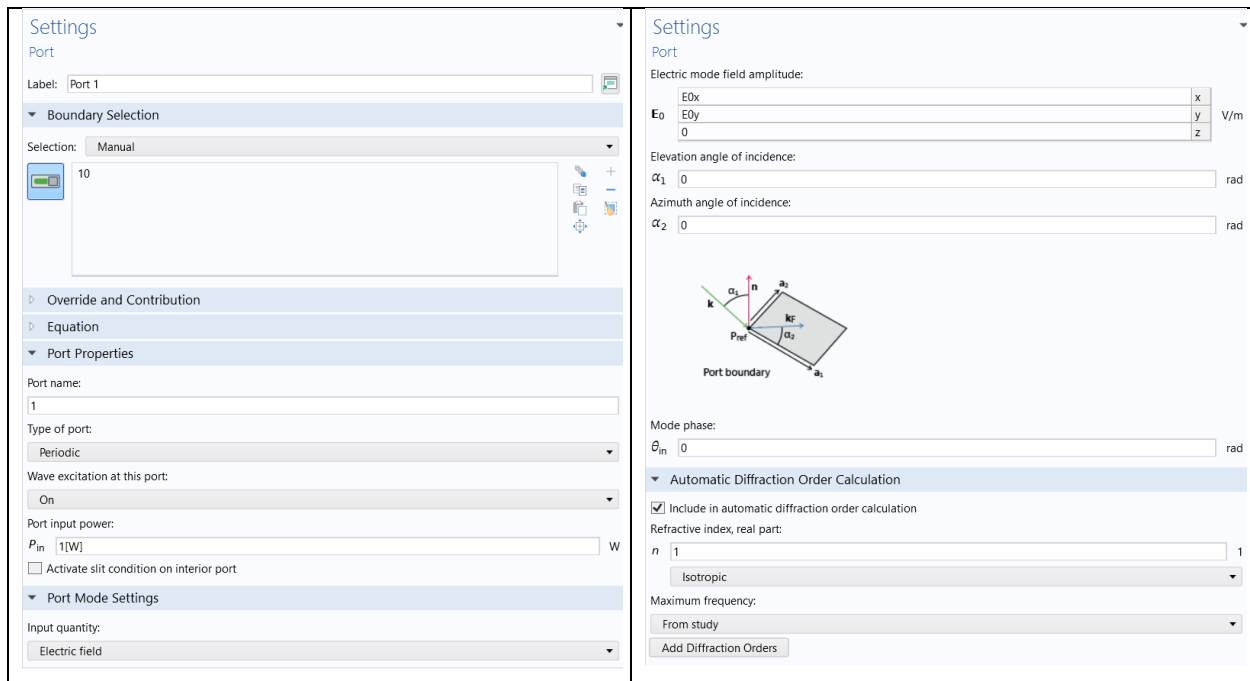


Figure S8. Settings for the “Port 1” layer of the “Electromagnetic Waves, Frequency Domain” layer.

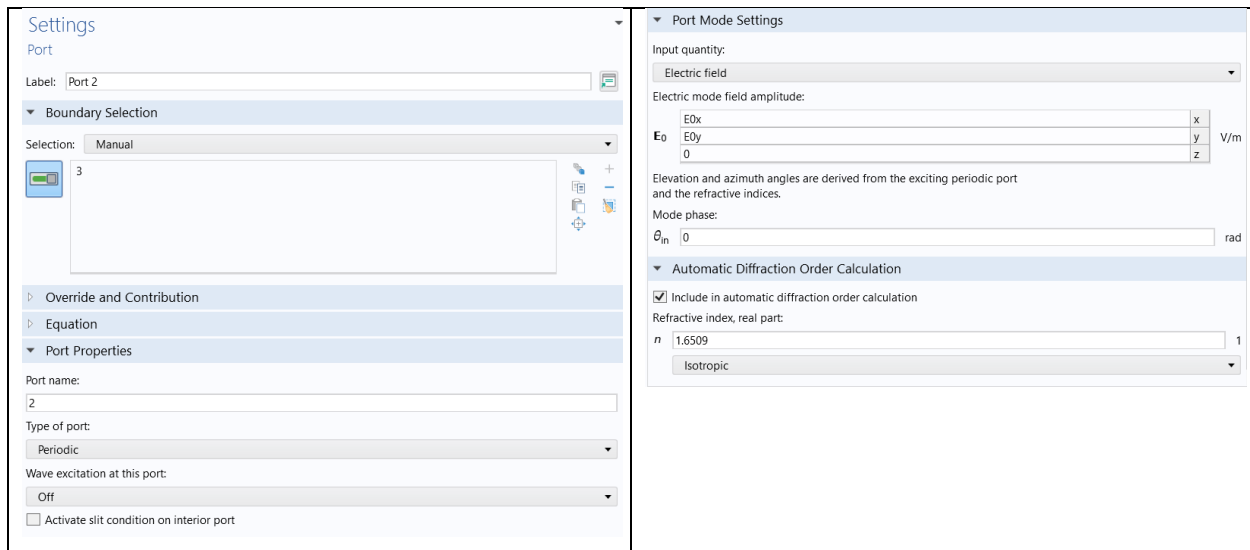


Figure S9. Settings of “Port 2” layer of the “Electromagnetic Waves, Frequency Domain” layer.

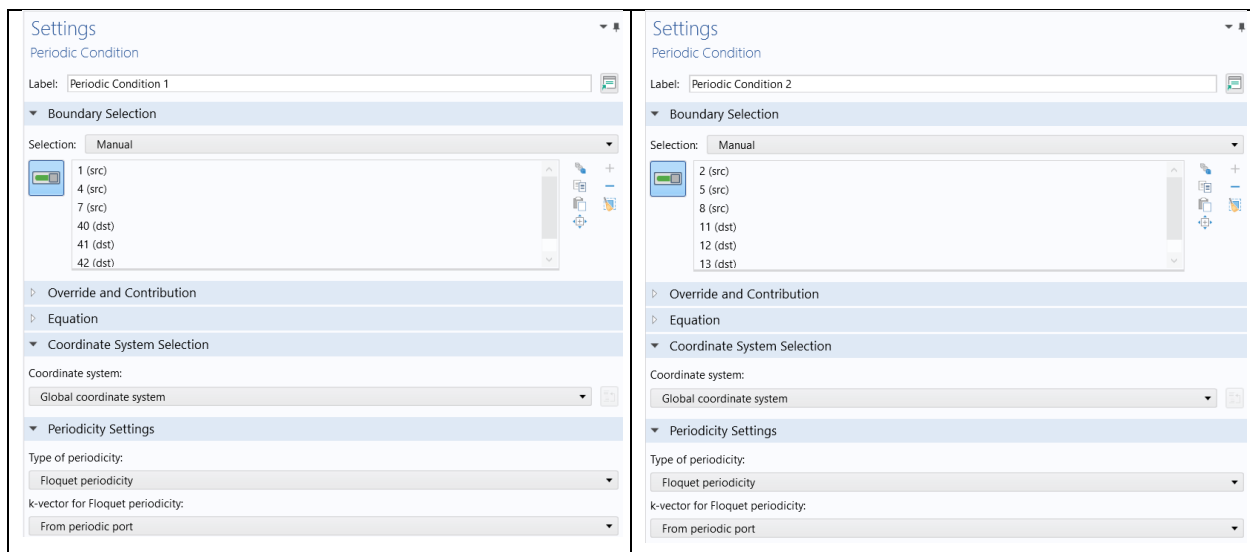


Figure S10. Settings for the **(Left)** “Periodic Condition 1” layer and the **(Right)** “Periodic Condition 2” layer of the parent “Electromagnetic Waves, Frequency Domain” layer. For both layers, “Floquet periodicity” is selected for the “Type of periodicity”.

S1.2.5: Mesh

The “Physics-controlled mesh” was chosen for “Sequence type:”. The chosen “Element size:” was “Normal”. Settings and mesh can be seen in Figure S11.



Figure S11. Settings of (*Left*) “Mesh” and (*Right*) the actual mesh of the model. The mesh layer is a child of “Component 1”.

Section S2: Predicting structural colour outputs

The reflectance spectra generated from section 1 were utilised to predict the structural colour output on the CIE 1931 2° Standard Observer colour space [6,7]. The XYZ tristimulus values quantify the amount of red, green, and blue recorded by the human eye and were calculated using the following equations:

$$X = k \sum_{\lambda} \phi_{\lambda}(\lambda) \bar{x}(\lambda) \Delta\lambda \quad (1)$$

$$Y = k \sum_{\lambda} \phi_{\lambda}(\lambda) \bar{y}(\lambda) \Delta\lambda \quad (2)$$

$$Z = k \sum_{\lambda} \phi_{\lambda}(\lambda) \bar{z}(\lambda) \Delta\lambda \quad (3)$$

The spectral distribution for a wavelength λ was denoted by $\phi_{\lambda}(\lambda)$, [8], where λ ranged between 400 nm and 700 nm. \bar{x} , \bar{y} , and \bar{z} represent the colour matching functions of a standard colorimetric observer (Figure S12) [9]. $\Delta\lambda = 1 \text{ nm}$ denotes the step-size used for the wavelength measurements [8]. The constant k was chosen such that $Y = 100$ for objects with reflectance equal to 1.0 across all wavelengths [8]:

$$k = \frac{100}{\sum_{\lambda} S(\lambda) \bar{y}(\lambda) \Delta\lambda} \quad (4)$$

$S(\lambda)$ is the spectral distribution of a selected illuminant [8]; in this work, the D65 illuminant was chosen [10,11] (Figure S13).

From these values, the (x, y) chromaticity coordinates were derived [12] using the following equation:

$$x = \frac{X}{X + Y + Z} \quad (5)$$

$$y = \frac{Y}{X + Y + Z} \quad (6)$$

These coordinates enable a two-dimensional representation of the colour specified by the tristimulus values on the CIE 1931 2° Standard Observer colour space [12,13].

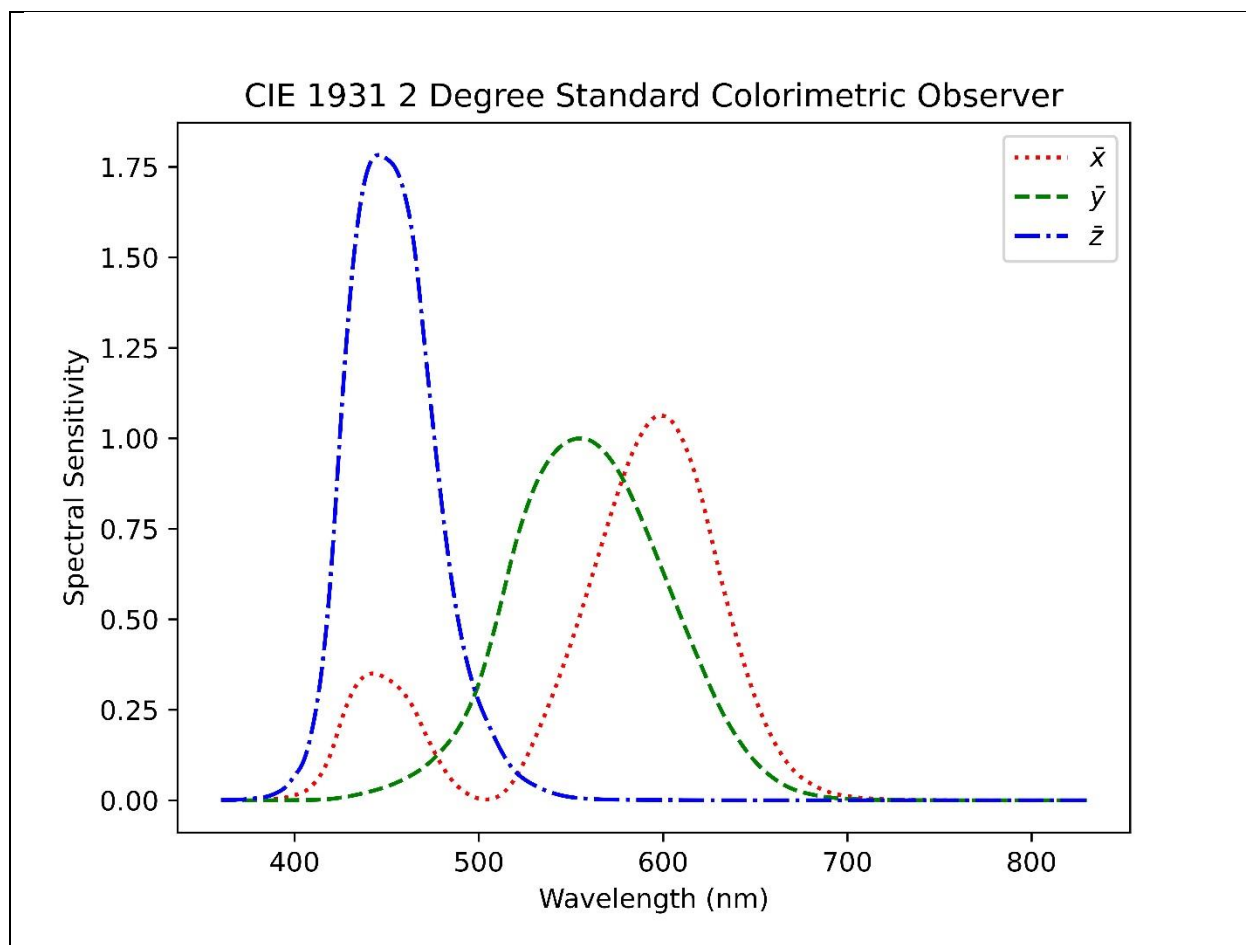


Figure S12. CIE 1931 2° degree standard colorimetric observer. Colour matching functions define how an observer’s visual system responds to red, green, and blue primaries [6,7]. The functions were derived by interpolating empirical measurements and are used to calculate tristimulus values [6–8]. The colour matching functions utilised in this study were obtained from an open-source Python library called Colour (see Section S7.1 for programming details) [9]; and cross-checked with those provided by the International Commission on Illumination [6,10,11].

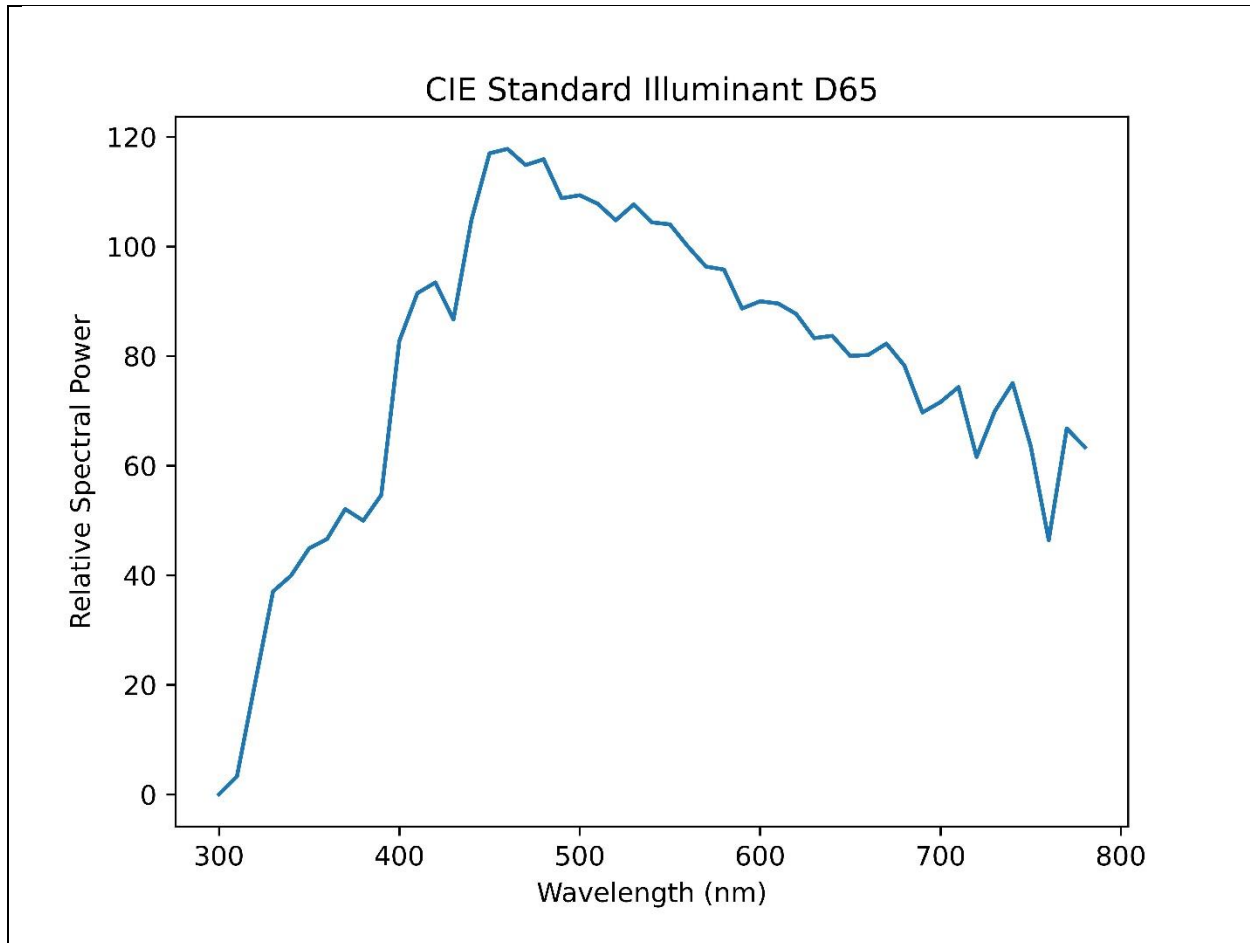


Figure S13. Relative spectral power distribution of the CIE standard illuminant D65. The CIE Standard Illuminant D65 represents average daylight in Northern and Western Europe, with a colour temperature of 6504 K [12,13]. Because it is an artificial illuminant, translation of our nanostructure arrays into the physical world is expected to yield a different colorimetric response under real light sources [14]. However, due to the challenges in obtaining tristimulus values for reflective media, such as our nanostructure arrays, we had to select a standard illuminant [14]. The choice of D65 is arbitrary. The illuminant spectrum was obtained from an open-source Python library called Colour (see Section S7.1 for programming details) [9]; and cross-checked with those provided by the International Commission on Illumination [15,16].

Section S3: Evaluating colour saturation

The calculated XYZ tristimulus values from section 2 were converted to the $L^*a^*b^*$ colour space (Section S3.1) [14,15]. The resulting $L^*a^*b^*$ values were used to determine the colour saturation, S_{LAB} , as ratio of chroma, C_{ab}^* , to lightness, L [16–19]:

$$S_{LAB} = \frac{C_{ab}^*}{L} = \frac{\sqrt{a^{*2} + b^{*2}}}{116 \left(\frac{Y}{Y_n} \right)^{\frac{1}{3}} - 16} \quad (7)$$

In the above equation, a^* and b^* correlate with red-green and blue-yellow chroma perceptions [15]. Y_n is the tristimulus Y value of the illuminant ($Y = 100$ for the D65 white point [20]) [11,15].

A qualitative comparison was conducted to assess the colour saturation of the colorimetric outputs of rectangle-shaped (or square-shaped) nanostructure arrays and their corresponding t-shaped nanostructure arrays. The authors are aware that Ref [19] finds discrepancies between this measure and the empirically-measured human perceptions of saturation. Nonetheless, saturation will be defined hereon as described above as it is the most accurate existing measure to the best of our knowledge.

Section S3.1: Calculating $L^*a^*b^*$ values

The L^* , a^* , and b^* quantities of the $L^*a^*b^*$ colour space correlate light-dark, red-green, and blue-yellow chroma perceptions, respectively. They are defined as follows [14,15]:

$$L^* = 116 f \left(\frac{Y}{Y_n} \right) - 16 \quad (8)$$

$$a^* = 500 \left[f \left(\frac{X}{X_n} \right) - f \left(\frac{Y}{Y_n} \right) \right] \quad (9)$$

$$b^* = 200 \left[f \left(\frac{Y}{Y_n} \right) - f \left(\frac{Z}{Z_n} \right) \right] \quad (10)$$

$$f(\omega) = \begin{cases} \omega^{\frac{1}{3}}, & \omega > \left(\frac{24}{116} \right)^3 \\ \left(\frac{841}{108} \right) \omega + \frac{16}{116}, & \omega \leq \left(\frac{24}{116} \right)^3 \end{cases} \quad (11)$$

In equations 8-10, $X_n = 95.04$, $Y_n = 100.00$, and $Z_n = 108.88$ are the tristimulus values of the D65 white point [20].

Section S4: Rectangle-shaped nanostructure arrays

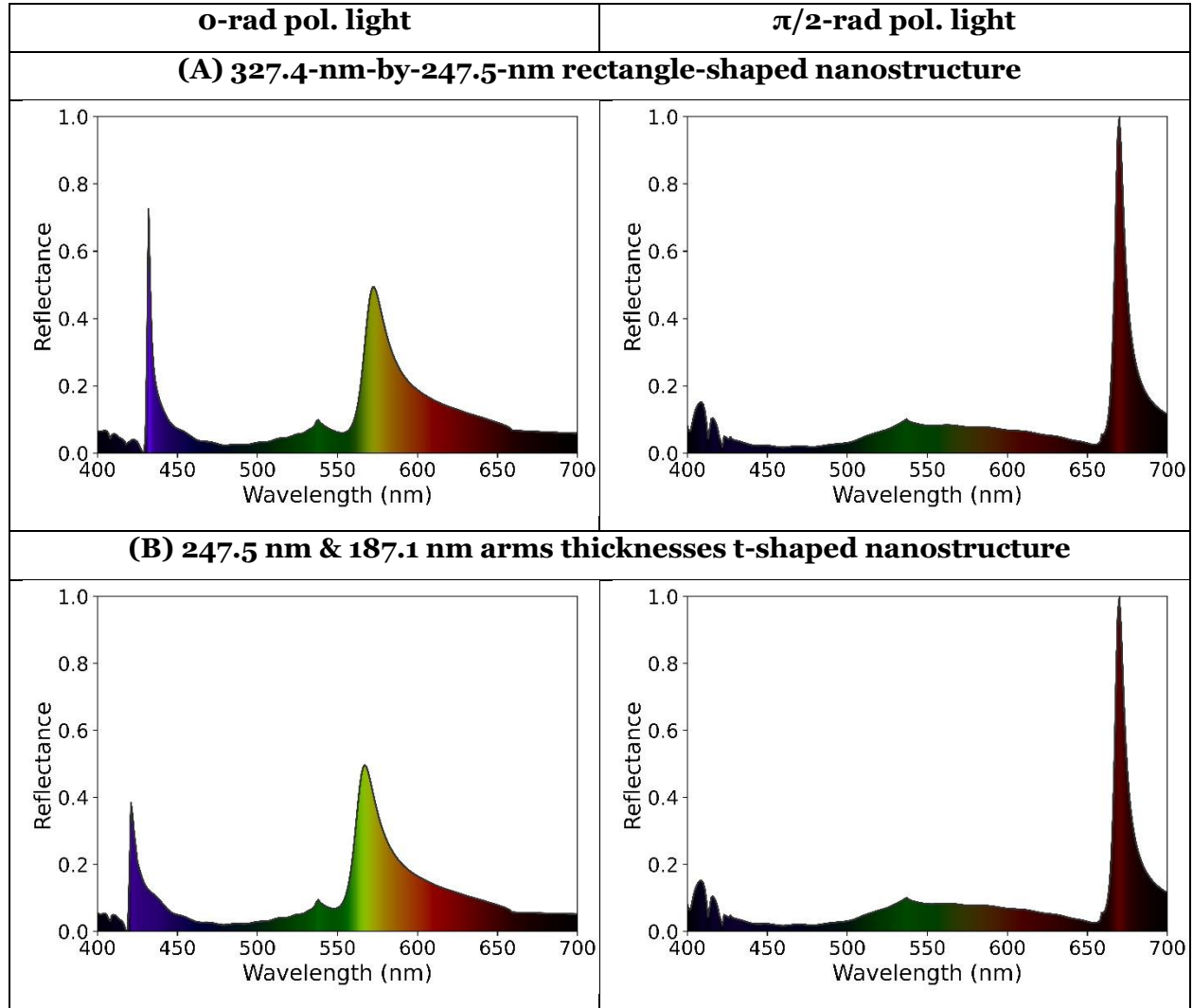
The length and width dimensions per aspect ratio of the rectangle-shaped nanostructure arrays (see Main Text, Results, Section 2) were chosen to keep a constant volume of $16,537,500 \text{ nm}^3$ [= $270 \text{ nm} \times \text{length} \times \text{width}$]. This was done to control for any effects the volume may have on the arising resonances, as per the advice of Ref. [21]. The exact geometric parameters are listed in Table S5.

Table S5. Length and width parameters for the simulated rectangle nanostructures seen in Section 2 of the Results in the Main Text.

Aspect Ratio	1:1	1:1.25	1:1.5	1:1.75	1:2
Length (nm)	247.5	276.7	303.1	327.4	350.0
Width (nm)	247.5	221.4	202.1	187.1	175.0
Height (nm)	270	270	270	270	270

Section S5: Rectangle-bound t-shaped nanostructure arrays

Figure S15 shows the reflectance spectra of the 0-rad and $\pi/2$ -rad linearly polarised light excitation of a rectangle-shaped nanostructure array (Figure S15A) and the corresponding t-shaped nanostructure arrays (Figures S15B-D), which corresponds to results reported in the Main Text.



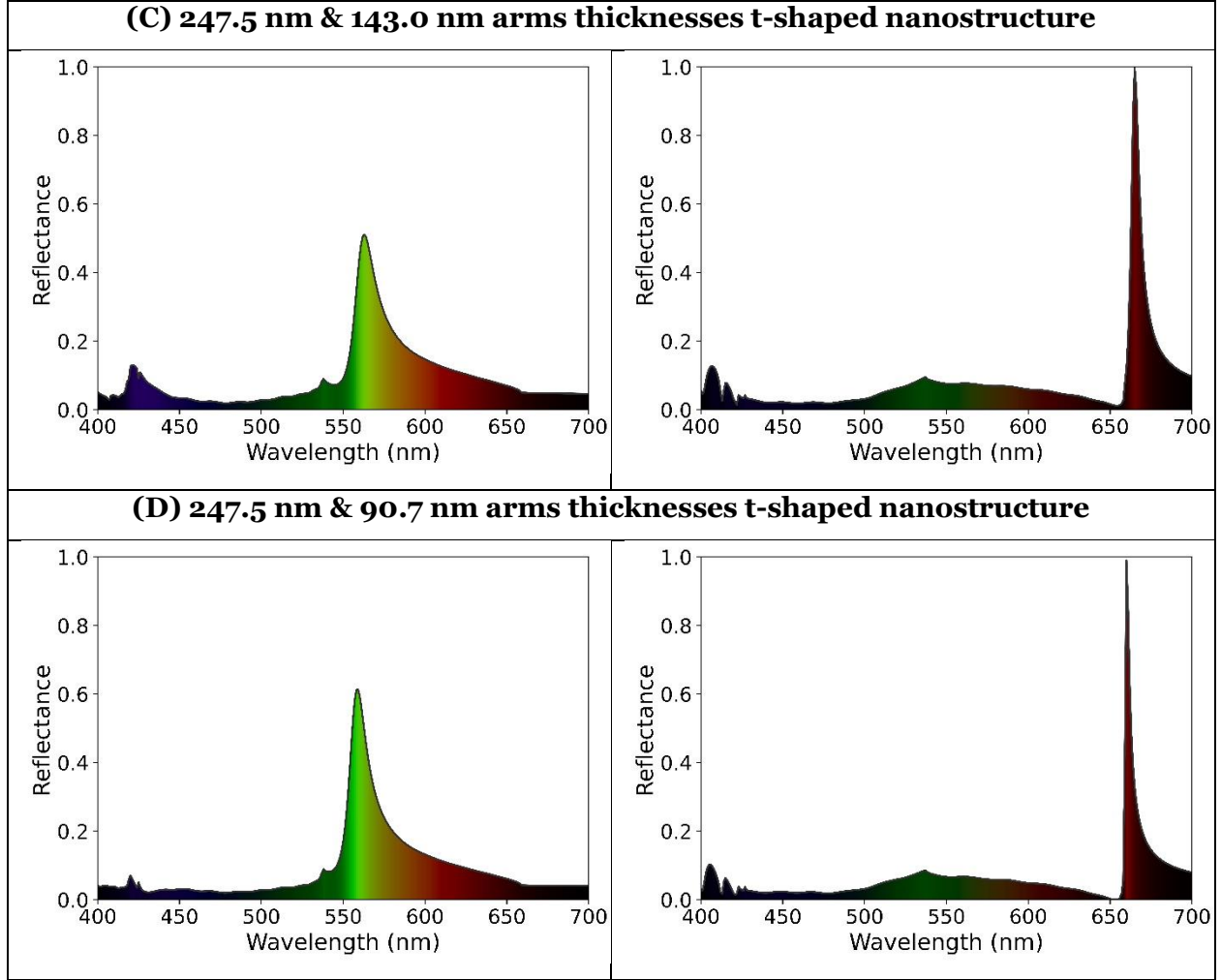


Figure S15. Reflectance plots of **(A)** rectangle-shaped and **(B-D)** t-shaped nanostructure arrays with 327.4-nm-by-247.5-nm bounds under (Left) 0-rad and (Right) $\pi/2$ -rad linearly polarised light excitation. **Left:** (A) HRW: 432 nm, FRW: 572 nm, FWHM: 24 nm; (B) HRW: 421 nm, FRW: 567 nm, FWHM: 24 nm; (C) HRW: 421 nm, FRW: 563 nm, FWHM: 21 nm; (D) FRW: 559 nm, FWHM: 17 nm. **Right:** (A) FRW: 676 nm, FWHM: 8 nm; (B) FRW: 670 nm, FWHM: 8 nm; (C) FRW: 665 nm, FWHM: 7 nm; (D) FRW: 660 nm, FWHM: 4 nm. Abbreviations: FRW: Fundamental resonance wavelength; FWHM: Full width at half-maximum (of fundamental resonance); HRW: High-order resonance wavelength.

Section S6: Square-bound t-shaped nanostructure arrays

Section S6.1: Square-shaped nanostructure arrays

The main text highlights results from rectangle-shaped nanostructure arrays and their corresponding t-shape nanostructure arrays for the development of two-colour-bound sensors of incident polarised light. However, we also performed our experiments with square-shaped nanostructure arrays and their corresponding t-shape nanostructure arrays for the development of monochromatic pixel arrays. Figure S16 displays the setup, mechanism, and physics of square-shaped nanostructure arrays, which mimic those of the rectangle-shaped nanostructure arrays shown in the main text.

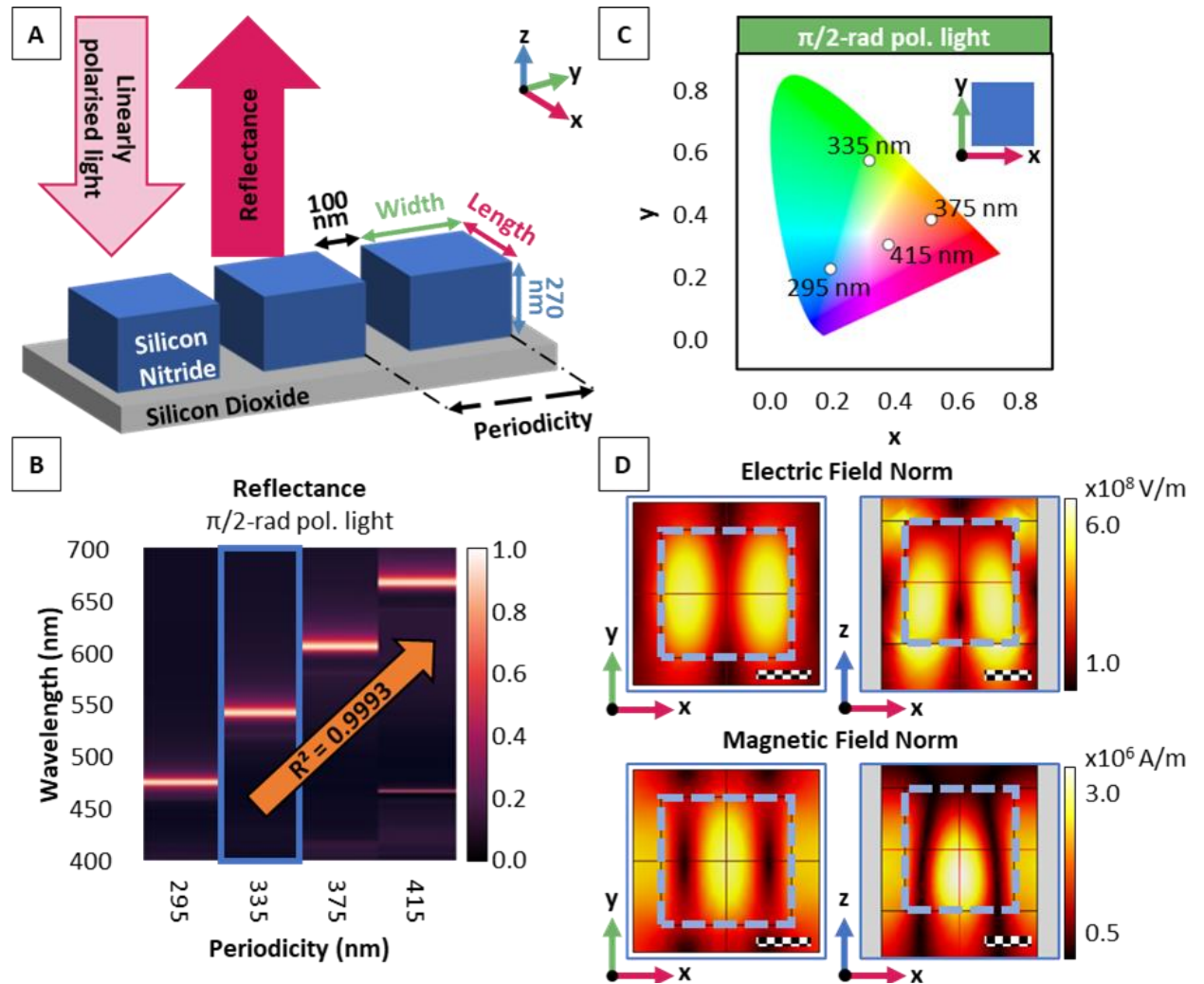


Figure S16. (A) Schematic of silicon nitride lattice resonant metasurface comprised of square-shaped nanostructures on a silicon dioxide substrate. (B) Heatmaps showing the reflectance spectra of square-shaped nanostructure arrays with periodicities of 295 nm, 335 nm, 375 nm, and 415 nm acquired by excitation with $\pi/2$ rad (x-axis) linearly polarised light. The 415-nm periodicity array displayed a high-order resonance at 466 nm. The orange arrow indicates shift of fundamental resonance wavelength with increasing periodicity. (C) Colorimetric output predicted from each reflectance spectrum plotted on the CIE 1931 2° Standard Observer colour space, illustrating the shift from blue to green to red as periodicity increases. (D) Near-field electric (top) and magnetic (bottom) norm plots of the 335-nm periodicity array. Checkered scale bars represent 100 nm.

Section S6.2: Cutting corners of square-shaped nanostructures

Using a 327.4-nm-by-327.4-nm square-shaped nanostructure array as a control, two resonance peaks were observed under excitation by linearly polarised light at 0 rad (Figure S17A): a high-order resonance at 481 nm with amplitude 0.89 and a fundamental resonance at 685 nm with amplitude 1.0. By cutting the corners of the nanostructures, a t-shaped nanostructure array with nanostructure arm thicknesses of 234.4 nm along both the vertical and horizontal axes was created (Figure S17B). This modification resulted in a blue-shift of the high-order and fundamental resonance peaks to 469 nm with amplitude 0.37 and 676 nm with amplitude 0.99, respectively. A second corner cut of the t-shape to arm thicknesses of 162.6 nm and 234.4 nm along the vertical and horizontal axes (Figure S17C) maintained the high-order resonance peak at 469 nm with amplitude 0.14 and the fundamental resonance peak at 668 nm with amplitude 1.0. A third corner cut of the t-shape to arm thicknesses of 162.6 nm along both the vertical and horizontal axes (Figure S17D) extinguished the high-order resonance and blue-shifted the fundamental resonance peak to 660 nm with amplitude 0.50.

Examining the electric field norms of the four nanostructure arrays at the high-order resonance peaks (Figures S17E-H, Left), revealed a decrease in the maximum value from 1.03E9 V/m with the control structure to 6.94E8 V/m, 3.61E8 V/m, and 1.7E8 with the first, second, and third corner-cut structures, respectively. In contrast, the electric field norms of the four nanostructure arrays at the fundamental resonance peaks (Figure S17E-H, Right) showed a maximum value of 4.81E8 V/m with the control structure and maximum values of 5.4E8 V/m, 5.77E8 V/m, and 5.31E8 V/m with the first, second, and third corner-cut structures, respectively. The high-order resonances exhibited activities centred at the corners and centres of the nanostructures, while the fundamental resonances showed activity only in the centres of the nanostructures.

Exciting the control and first corner-cut nanostructure arrays with linearly polarised light at angles of 0 rad, $\pi/6$ rad, $\pi/4$ rad, $\pi/3$ rad, and $\pi/2$ rad resulted in identical reflectance spectra across all polarisations (Figures S18A and S18B). The colorimetric output of these spectra on the CIE 1931 2° Standard Observer colour space appeared as a single point (Figures S18C and S18D).

In contrast, exciting the second corner-cut nanostructure array, where the corners were asymmetrically cut, with linearly polarised light resulted in hybrid signals comprising resonances from the 0 rad and $\pi/2$ rad polarisations (Figure S18E). The 0 rad polarisation displayed a high-order resonance whereas the $\pi/2$ rad polarisation did not. These hybrid signals were amplitude-adjusted based on the angular deviation from the 0 rad or $\pi/2$ rad axes. The colorimetric output

of these spectra on the CIE 1931 2° Standard Observer colour space appeared on a line bounded between the colorimetric outputs of the 0 rad and $\pi/2$ rad polarisations (Figure S18F).

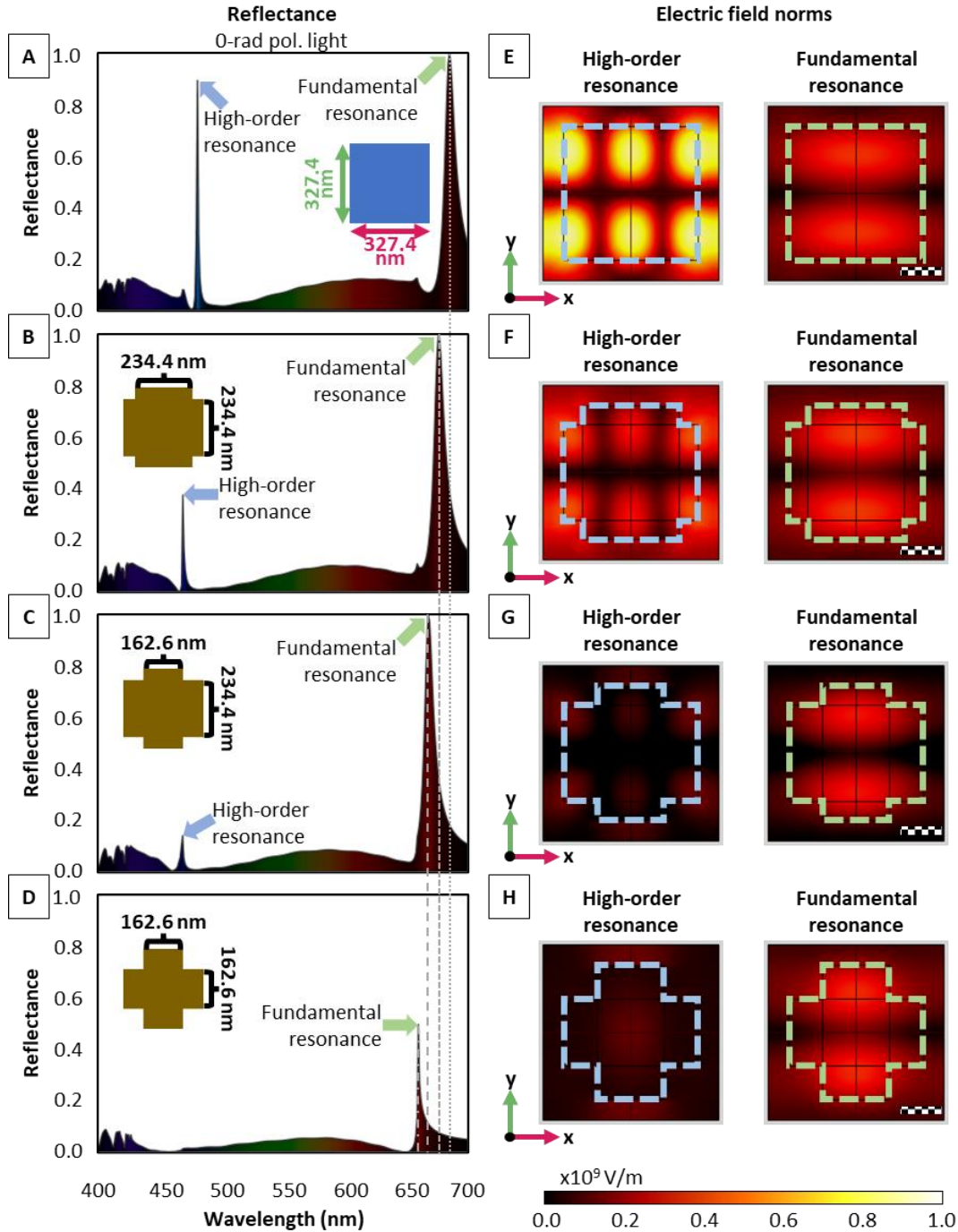


Figure S17. (A-D) Reflectance spectra of square-shaped and t-shaped nanostructure arrays, indicated by insets, under 0 rad (y-axis) linearly polarised light excitation. Green arrows highlight the location of the fundamental resonance wavelength. Blue arrows highlight the location of the high-order resonance wavelength. The dotted, short dashed, long dashed, and dash-dotted lines indicate the position of the fundamental resonance wavelength, which is blue-shifted when transforming a square-shaped nanostructure array to a t-shaped nanostructure array. (E-H) Near-field plots of the electric field norm of the (Left) high-order and (Right) fundamental resonances of the square-shaped and t-shaped nanostructure arrays. Checkered scale bars are 100 nm.

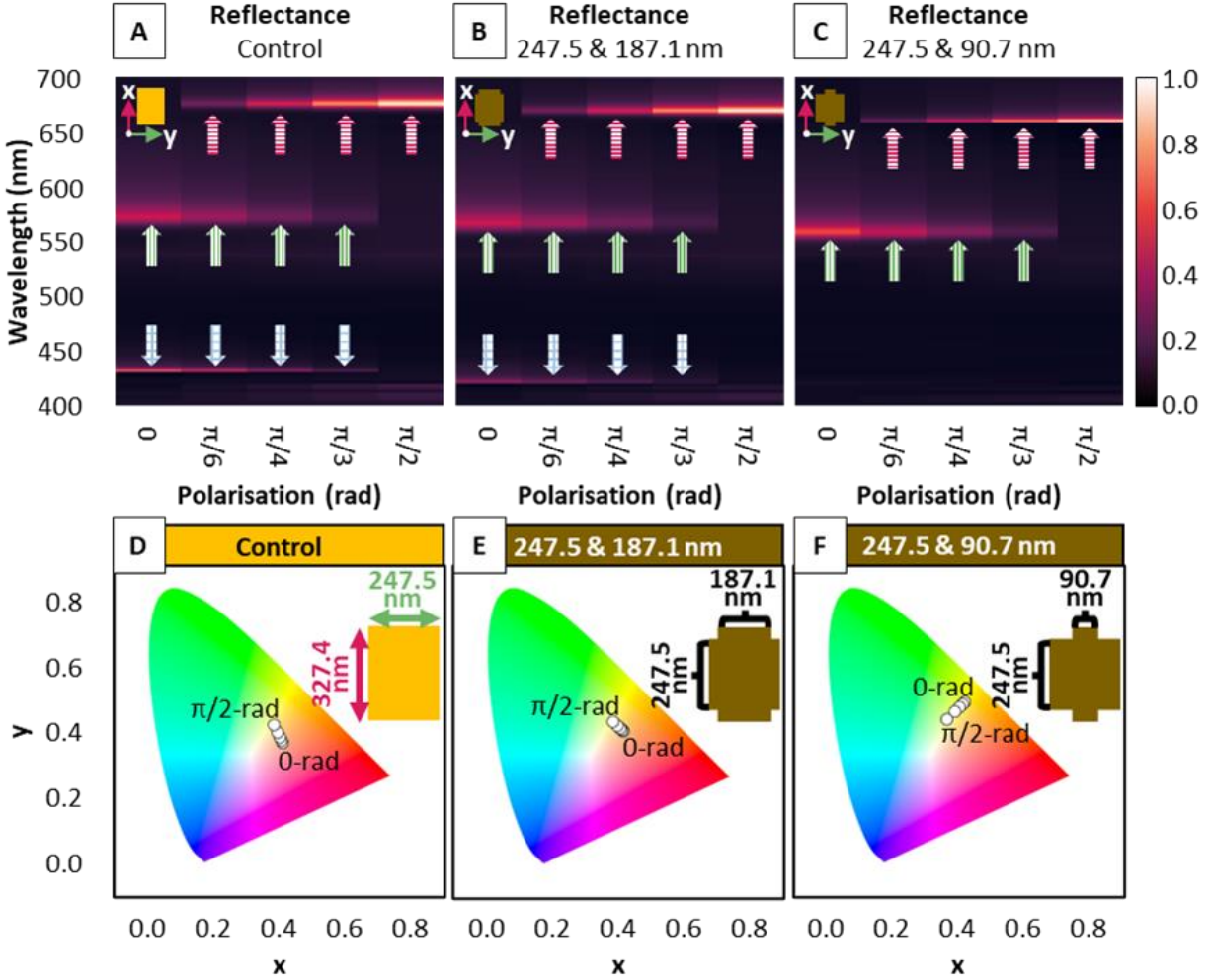


Figure S18. (A-C) Reflectance heatmaps acquired from the rectangle-shaped and t-shaped nanostructure arrays from Figure 3. Insets indicate the type of nanostructure. Blue, grid-filled arrows indicate the high-order resonances. Green, vertically striped arrows indicate fundamental resonance signals shared with the 0 rad (y-axis) polarisation. Red, horizontally striped arrows indicate fundamental resonance signals shared with the $\pi/2$ rad (x-axis) polarisation. The high-order resonances vanished with the t-shaped nanostructure array in (C). (D-F) Colorimetric output predicted from each reflectance spectrum in (A-C) plotted on the CIE 1931 2° Standard Observer colour space. Only the 0 rad (y-axis) and $\pi/2$ rad (x-axis) polarisations are labelled. All outputs are bounded along a line. The lines in (D, F) have a diagonal orientation. The line in (F) has an anti-diagonal orientation.

Section S6.4: Saturation scores of square-bound nanostructure arrays

The colour saturation was calculated as described in Section S3 of this document and shown in Figure S19. In the square-bound t-shaped structures, both the 0 rad polarisation and $\pi/2$ rad polarisation exhibited high-order and fundamental resonances (see Supplementary

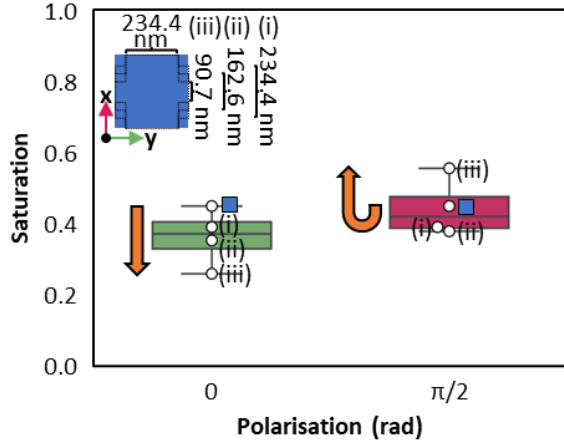
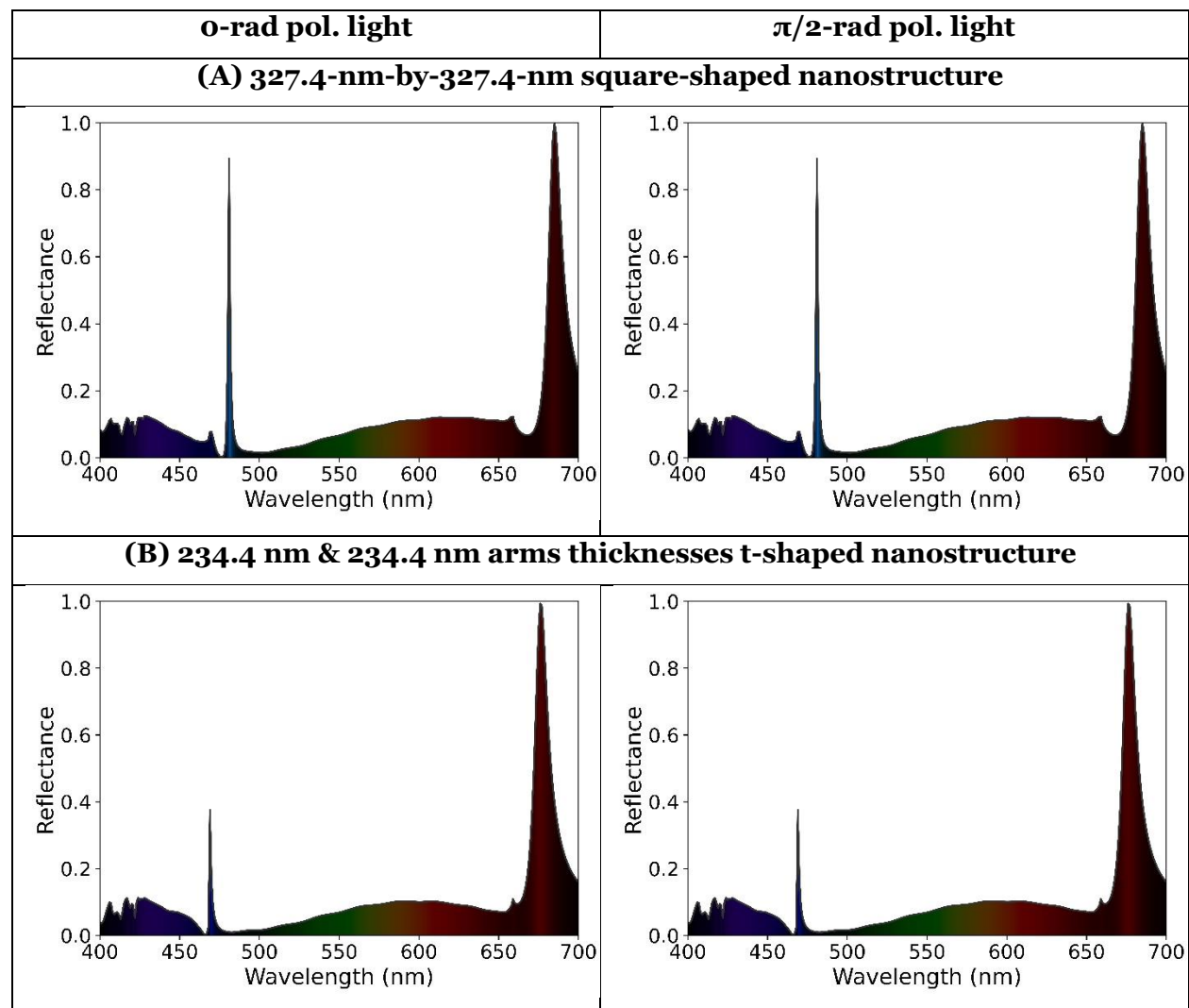


Figure S19. Box-and-whisker plot illustrating colour saturation measurements of square-bound nanostructure arrays under 0 rad (y-axis) and $\pi/2$ rad (x-axis) linearly polarised light excitation. (i), (ii), and (iii) indicate t-shape structures where (i) has the smallest area of corners removed and (iii) with the largest area of corners removed (exact dimensions provided in insets). Orange arrows indicate movement from the square-shaped control to the t-shape with the greatest area of corners cut out. Boxes represent the quartiles, with the horizontal grey line indicating the median. Whiskers represent the range of the distribution.

Material, Section S6.5 for corresponding reflectance spectra). Under 0 rad polarisation, the colour saturation decreased as the area of the removed corners increased. Under $\pi/2$ rad polarisation, the colour saturation only showed an increase when the largest area of the corners was removed, while the other t-shaped structures showed a decrease in colour saturation compared to the control. This decrease in colour saturation is attributed to (i) the reduced capability of these nanostructures to support the fundamental resonance across a wider range of wavelengths, evidenced by a decrease in the full-width at half maximum of these resonances (see caption in Supplementary Material, Figure S20), and (ii) the failure to extinguish the high-order resonances (Figures S17A-C). Figure S17D showed the dampening consequence of cutting the corners too close to the activity region of the fundamental resonance.

Section S6.5: Orthogonal polarisations reflectance spectra

Figure S19 shows the reflectance spectra of the o-rad and $\pi/2$ -rad linearly polarised light excitation of a square-shaped nanostructure array (Figure S16A) and the corresponding t-shaped nanostructure arrays (Figures S16B-D). These results are not reported in the main text.



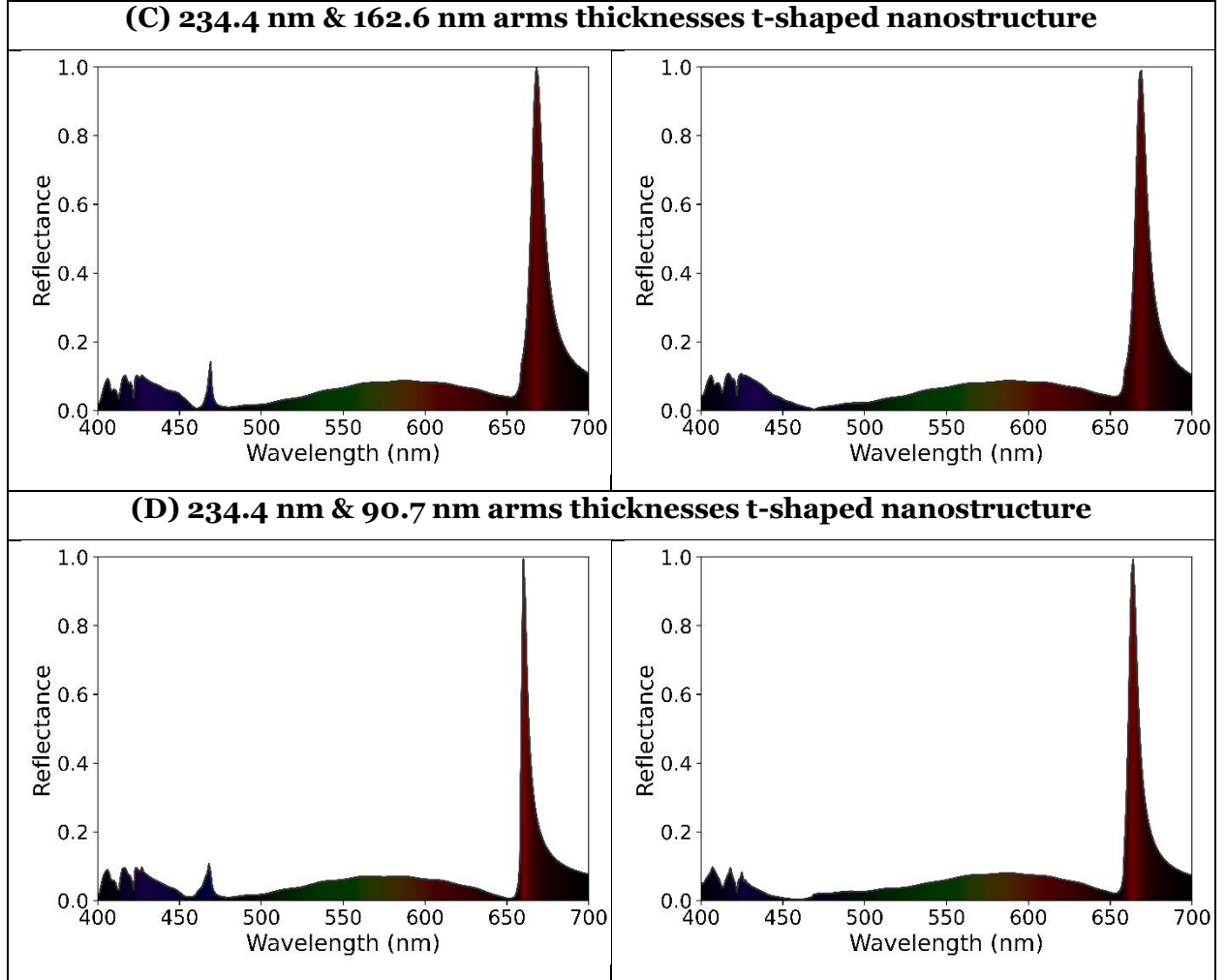


Fig. S20: Reflectance plots of **(A)** square-shaped and **(B-D)** t-shaped nanostructure arrays with 327.4-nm-by-327.4-nm bounds under (Left) o-rad and (Right) $\pi/2$ -rad linearly polarised light excitation. **Left:** (A) HRW: 481 nm, FRW: 685 nm, FWHM: 11 nm; (B) HRW: 469 nm, FRW: 676 nm, FWHM: 11 nm; (C) HRW: 469 nm, FRW: 668 nm, FWHM: 10 nm; (D) HRW: 468 nm, FRW: 660 nm, FWHM: 4 nm. **Right:** (A) HRW: 481 nm, FRW: 685 nm, FWHM: 11 nm; (B) HRW: 469 nm, FRW: 676 nm, FWHM: 11 nm; (C) FRW: 669 nm, FWHM: 9 nm; (D) FRW: 664 nm, FWHM: 7 nm. Abbreviations: FRW: Fundamental resonance wavelength; FWHM: Full width at half-maximum (of fundamental resonance); HRW: High-order resonance wavelength.

Section S7: Programming Scripts

All programming scripts and environments are provided in the “Workflow/Programming/” folder. Within this folder are the “Python” (Section S7.1) and “Mathematica” (Section S7.2) sub-folders.

Section S7.1: Python

Conda v22.11.1 [22] installed using the Miniconda package [23] by Anaconda Software Distribution [24] was utilised to create a virtual programming environment. Within this environment, Python v3.10.8 [25,26] was installed. This Python version, in conjunction with several open-source libraries, was used for the calculations and plots presented in the Main Text. The primary libraries used were Colour v0.4.2 [27], Matplotlib v3.6.2 [28,29], Numpy v1.23.5 [30,31], Pandas v1.5.2 [32,33], and Seaborn v0.12.2 [34]. A full list of packages and dependencies installed within the Conda environment can be found in Section S7.1.2.

The Conda environment file is provided as “20230718_CuttingCorners_CondaEnvironment.yml”. Instructions for activating this environment can be found in Ref. [35].

In addition, three Python files are provided:

1. “Main.py”: Central hub for analysing and plotting the generated data.
2. “SpectralAnalysis.py”: Implements a Spectrum class to keep track of a given spectrum’s metadata and resultant calculations.
3. “ColourPlotTemplates.py”: Provides functions for visualising the data extracted from a spectrum or spectra.’

All programming for this section was completed on Ubuntu 22.04.1 LTS [36] installed in the WLS2 environment of Windows 10 [37].

Section S7.1.2: Python Packages & Dependencies

```
# packages in environment at /home/██████████/.conda/envs/DataScience_env:
#
# Name                                Version                                Build      Channel
_libgcc_mutex                        0.1                                    main
_openmp_mutex                        5.1                                   1_gnu
astroid                              2.11.7                                py310h06a4308_0  anaconda
asttokens                            2.2.1                                pyhd8ed1ab_0    conda-forge
backcall                             0.2.0                                pyh9f0ad1d_0    conda-forge
backports                            1.0                                   pyhd8ed1ab_3    conda-forge
backports.functools_lru_cache        1.6.4                                pyhd8ed1ab_0    conda-forge
beartype                             0.11.0                               pyhd8ed1ab_0    conda-forge
blas                                 1.0                                   mk1
bottleneck                           1.3.5                                py310ha9d4c09_0
brotli                              1.0.9                                h5eee18b_7
brotli-bin                           1.0.9                                h5eee18b_7
bzip2                                1.0.8                                h7b6447c_0
ca-certificates                      2022.12.7                            ha878542_0      conda-forge
```

Z.H., S.K., L.V.P., Cutting corners to suppress high-order modes in Mie resonator arrays

certifi	2022.12.7	pyhd8ed1ab_0	conda-forge
colour-science	0.4.2	pyh6c4a22f_0	conda-forge
contourpy	1.0.5	py310hdb19cb5_0	
cycler	0.11.0	pyhd3eb1b0_0	
dbus	1.13.18	hb2f20db_0	
debugpy	1.5.1	py310h295c915_0	
decorator	5.1.1	pyhd8ed1ab_0	conda-forge
dill	0.3.4	pyhd3eb1b0_0	anaconda
executing	1.2.0	pyhd8ed1ab_0	conda-forge
expat	2.4.9	h6a678d5_0	
fftw	3.3.9	h27cfd23_1	
fontconfig	2.14.1	h52c9d5c_1	
fonttools	4.25.0	pyhd3eb1b0_0	
freetype	2.12.1	h4a9f257_0	
geos	3.8.0	he6710b0_0	
giflib	5.2.1	h7b6447c_0	
glib	2.69.1	he621ea3_2	
gst-plugins-base	1.14.0	h8213a91_2	
gstreamer	1.14.0	h28cd5cc_2	
icu	58.2	he6710b0_3	
imageio	2.25.0	pyh24c5eb1_0	conda-forge
importlib-metadata	6.0.0	pyha770c72_0	conda-forge
importlib_metadata	6.0.0	hd8ed1ab_0	conda-forge
intel-openmp	2021.4.0	h06a4308_3561	
ipykernel	6.15.0	pyh210e3f2_0	conda-forge
ipython	8.10.0	pyh41d4057_0	conda-forge
isort	5.9.3	pyhd3eb1b0_0	anaconda
jedi	0.18.2	pyhd8ed1ab_0	conda-forge
joblib	1.1.1	py310h06a4308_0	
jpeg	9e	h7f8727e_0	
jupyter_client	8.0.3	pyhd8ed1ab_0	conda-forge
jupyter_core	4.12.0	py310hff52083_0	conda-forge
kiwisolver	1.4.4	py310h6a678d5_0	
krb5	1.19.2	hac12032_0	
lazy-object-proxy	1.6.0	py310h7f8727e_0	anaconda
lcms2	2.12	h3be6417_0	
ld_impl_linux-64	2.38	h1181459_1	
lerc	3.0	h295c915_0	
libbrotlicommon	1.0.9	h5eee18b_7	
libbrotlidec	1.0.9	h5eee18b_7	
libbrotlienc	1.0.9	h5eee18b_7	
libclang	10.0.1	default_hb85057a_2	
libdeflate	1.8	h7f8727e_5	
libedit	3.1.20221030	h5eee18b_0	
libevent	2.1.12	h8f2d780_0	
libffi	3.4.2	h6a678d5_6	
libgcc-ng	11.2.0	h1234567_1	
libgfortran-ng	11.2.0	h00389a5_1	
libgfortran5	11.2.0	h1234567_1	
libgomp	11.2.0	h1234567_1	
libllvm10	10.0.1	hbc73fb_5	
libpng	1.6.37	hbc83047_0	
libpq	12.9	h16c4e8d_3	
libsodium	1.0.18	h36c2ea0_1	conda-forge
libstdcxx-ng	11.2.0	h1234567_1	
libtiff	4.5.0	hecacb30_0	
libuuid	1.41.5	h5eee18b_0	

Z.H., S.K., L.V.P., Cutting corners to suppress high-order modes in Mie resonator arrays

libwebp	1.2.4	h11a3e52_0	
libwebp-base	1.2.4	h5eee18b_0	
libxcb	1.15	h7f8727e_0	
libxkbcommon	1.0.1	hfa300c1_0	
libxml2	2.9.14	h74e7548_0	
libxslt	1.1.35	h4e12654_0	
lz4-c	1.9.4	h6a678d5_0	
matplotlib	3.6.2	py310h06a4308_0	
matplotlib-base	3.6.2	py310h945d387_0	
matplotlib-inline	0.1.6	pyhd8ed1ab_0	conda-forge
mccabe	0.7.0	pyhd3eb1b0_0	anaconda
mk1	2021.4.0	h06a4308_640	
mk1-service	2.4.0	py310h7f8727e_0	
mk1_fft	1.3.1	py310hd6ae3a3_0	
mk1_random	1.2.2	py310h00e6091_0	
munkres	1.1.4	py_0	
ncurses	6.3	h5eee18b_3	
nest-asyncio	1.5.6	pyhd8ed1ab_0	conda-forge
nspr	4.33	h295c915_0	
nss	3.74	h0370c37_0	
numexpr	2.8.4	py310h8879344_0	
numpy	1.23.5	py310hd5efca6_0	
numpy-base	1.23.5	py310h8e6c178_0	
openssl	1.1.1t	h7f8727e_0	
packaging	22.0	py310h06a4308_0	
pandas	1.5.2	py310h1128e8f_0	
parso	0.8.3	pyhd8ed1ab_0	conda-forge
pcre	8.45	h295c915_0	
pep8	1.7.1	py310h06a4308_1	anaconda
pexpect	4.8.0	pyh1a96a4e_2	conda-forge
pickleshare	0.7.5	py_1003	conda-forge
pillow	9.3.0	py310hace64e9_1	
pip	22.3.1	py310h06a4308_0	
platformdirs	2.4.0	pyhd3eb1b0_0	anaconda
ply	3.11	py310h06a4308_0	
prompt-toolkit	3.0.36	pyha770c72_0	conda-forge
psutil	5.9.0	py310h5eee18b_0	
ptyprocess	0.7.0	pyhd3deb0d_0	conda-forge
pure_eval	0.2.2	pyhd8ed1ab_0	conda-forge
pygments	2.14.0	pyhd8ed1ab_0	conda-forge
pylint	2.14.5	py310h06a4308_0	anaconda
pyparsing	3.0.9	py310h06a4308_0	
pyqt	5.15.7	py310h6a678d5_1	
pyqt5-sip	12.11.0	pypi_0	pypi
python	3.10.8	h7a1cb2a_1	
python-dateutil	2.8.2	pyhd3eb1b0_0	
python_abi	3.10	2_cp310	conda-forge
pytz	2022.7	py310h06a4308_0	
pyzmq	23.2.0	py310h6a678d5_0	
qt-main	5.15.2	h327a75a_7	
qt-webengine	5.15.9	hd2b0992_4	
qtwebkit	5.212	h4eab89a_4	
readline	8.2	h5eee18b_0	
scikit-learn	1.2.0	py310h6a678d5_0	
scipy	1.9.3	py310hd5efca6_0	
seaborn	0.12.2	py310h06a4308_0	
setuptools	65.6.3	py310h06a4308_0	

shapely	1.8.4	py310h81ba7c5_0	
sip	6.6.2	py310h6a678d5_0	
six	1.16.0	pyhd3eb1b0_1	
sqlite	3.40.1	h5082296_0	
stack_data	0.6.2	pyhd8ed1ab_0	conda-forge
threadpoolctl	2.2.0	pyh0d69192_0	
tk	8.6.12	h1ccaba5_0	
toml	0.10.2	pyhd3eb1b0_0	
tomli	2.0.1	py310h06a4308_0	anaconda
tomlkit	0.11.1	py310h06a4308_0	anaconda
tornado	6.2	py310h5eee18b_0	
traitlets	5.9.0	pyhd8ed1ab_0	conda-forge
typing_extensions	4.3.0	py310h06a4308_0	anaconda
tzdata	2022g	h04d1e81_0	
wcwidth	0.2.6	pyhd8ed1ab_0	conda-forge
wheel	0.37.1	pyhd3eb1b0_0	
wrapt	1.14.1	py310h5eee18b_0	anaconda
xz	5.2.8	h5eee18b_0	
zeromq	4.3.4	h9c3ff4c_1	conda-forge
zipp	3.14.0	pyhd8ed1ab_0	conda-forge
zlib	1.2.13	h5eee18b_0	
zstd	1.5.2	ha4553b6_0	

Section S7.2: Mathematica

Wolfram notebook (extension: .nb) was used with Wolfram Mathematica v13.3.0.0 [38,39] for 64-bit Microsoft Windows 11. Colour matching functions and standard illuminant D65 values were imported from the online datasets provided by the International Commission on Illumination [40,41]. The analyses performed with Mathematica were not included in the Main Text; it was used as a qualitative validation of the analysis performed in Python (see Section S8.1).

Nevertheless, the Mathematica code is provided in a file named, “SpectralAnalysis.nb”. Further details of the code’s implementation are provided in Section S7.2.1.

Section S7.2.1: Code

The code within “SpectralAnalysis.nb” can be split into four sections (labelled within the code):

(i) “Import XYZ Functions and D65 White point”: imports and plots the colour matching functions and standard illuminant D65 values; and calculates the D65 tristimulus values normalised such that $Y=1$. To note, the tristimulus value calculations here do not consider the normalisation factor mentioned in Section 2 of the Main Text. Thus, values acquired from Mathematica can only be compared qualitatively and not quantitatively with those from Python.

(ii) “Define XYZ \rightarrow $L^*a^*b^*$ conversion with D65 reference white”: Converts the D65 tristimulus values from (i) to their corresponding L^* , a^* , and b^* quantities (see Main Text, Appendix, Section A1, Equations 8-11).

(iii) “COMSOL Data Import”: Imports the spectra data collected from the COMSOL Multiphysics® simulations.

(iv) “Calculate LAB co-ordinates of Spectra, their Distance to D65 and Saturation”: Calculates the L^* , a^* , and b^* quantities of the imported spectra and their corresponding saturation scores (see Main Text, Methods, Section 3, Equation 7). These results were exported out as .csv tables.

To note, this code provides additional data calculations and visualisations not described above. However, what is described above is predominantly what was used for the qualitative comparisons with the data processed in Python that was reported in the Main Text.

Section S8: Data

All data, found in the “Workflow/Data/” folder, is provided in either .txt or .csv format. Columns in .txt files are separated with space(s); columns in .csv files are separated by a comma (“,”). Each file contains four columns and a corresponding header. The attributes of each column are as follows:

1. Column #1: Wavelength(nm)
2. Column #2: Reflectance
3. Column #3: Transmittance
4. Column #4: Absorptance

There are a total of fifty-three files. The files are organised into appropriate folders titled “SquareShapedNanostructureArrays” (Section S8.1), “RectangleShapedNanostructureArrays” (Section S8.2), “RectangleBoundTShapedNanostructureArrays” (SectionS8.3), and “SquareBoundTShapedNanostructureArrays” (Section S8.4).

Section S8.1: Square-shaped nanostructure arrays

Four .csv files are provided containing reflectance, transmittance, and absorptance data of square-shaped nanostructure arrays excited by $\pi/2$ -rad linearly polarised light:

1. P195nm_SquareNanoarray_Study01_RTATable.csv
2. P235nm_SquareNanoarray_Study01_RTATable.csv
3. P275nm_SquareNanoarray_Study01_RTATable.csv
4. P315nm_SquareNanoarray_Study01_RTATable.csv

The number following the “P” flag in each file name corresponds to the periodicity of the array: 195 nm, 235 nm, 275 nm, or 315 nm.

Section S8.2: Rectangle-shaped nanostructure arrays

Thirteen .csv files are provided containing reflectance, transmittance, and absorptance data of rectangle-shaped nanostructure arrays excited by varying angles of linearly polarised light:

1. odegpol_RectangleNanoarray_Study00_RTATable.txt
2. odegpol_RectangleNanoarray_Study01_RTATable.txt
3. odegpol_RectangleNanoarray_Study02_RTATable.txt
4. odegpol_RectangleNanoarray_Study03_RTATable.txt
5. odegpol_RectangleNanoarray_Study04_RTATable.txt
6. 30degpol_RectangleNanoarray_Study01_RTATable.txt
7. 45degpol_RectangleNanoarray_Study01_RTATable.txt
8. 60degpol_RectangleNanoarray_Study01_RTATable.txt
9. 90degpol_RectangleNanoarray_Study00_RTATable.txt

10. 90degpol_RectangleNanoarray_Study01_RTATable.txt
11. 90degpol_RectangleNanoarray_Study02_RTATable.txt
12. 90degpol_RectangleNanoarray_Study03_RTATable.txt
13. 90degpol_RectangleNanoarray_Study04_RTATable.txt

File names containing:

- “0degpol” correspond to 0-rad linearly polarised light excitation.
- “30degpol” correspond to $\pi/6$ -rad linearly polarised light excitation.
- “45degpol” correspond to $\pi/4$ -rad linearly polarised light excitation.
- “60degpol” correspond to $\pi/3$ -rad linearly polarised light excitation.
- “90degpol” correspond to $\pi/2$ -rad linearly polarised light excitation.
- “Study00” correspond to the 247.5-nm-by-247.5-nm square-shaped nanostructure array (1:1 aspect ratio).
- “Study01” correspond to the 221.4-nm-by-276.7-nm rectangle-shaped nanostructure array (1:1.25 aspect ratio).
- “Study02” correspond to the 202.1-nm-by-303.1-nm rectangle-shaped nanostructure array (1:1.5 aspect ratio).
- “Study03” correspond to the 187.1-nm-by-327.4-nm rectangle-shaped nanostructure array (1:1.75 aspect ratio).
- “Study04” correspond to the 175-nm-by-350-nm rectangle-shaped nanostructure array (1:2 aspect ratio).

Section S8.3: Rectangle-bound t-shaped nanostructure arrays

Seventeen .txt files are provided containing reflectance, transmittance, and absorptance data of rectangle-bound nanostructure arrays excited by varying angles of linearly polarised light:

1. 0degpol_RectangleBoundTShapedNanoarray_Study00_RTATable.txt
2. 0degpol_RectangleBoundTShapedNanoarray_Study01_RTATable.txt
3. 0degpol_RectangleBoundTShapedNanoarray_Study02_RTATable.txt
4. 0degpol_RectangleBoundTShapedNanoarray_Study03_RTATable.txt
5. 30degpol_RectangleBoundTShapedNanoarray_Study00_RTATable.txt
6. 30degpol_RectangleBoundTShapedNanoarray_Study01_RTATable.txt
7. 30degpol_RectangleBoundTShapedNanoarray_Study03_RTATable.txt
8. 45degpol_RectangleBoundTShapedNanoarray_Study00_RTATable.txt
9. 45degpol_RectangleBoundTShapedNanoarray_Study01_RTATable.txt
10. 45degpol_RectangleBoundTShapedNanoarray_Study03_RTATable.txt
11. 60degpol_RectangleBoundTShapedNanoarray_Study00_RTATable.txt

12. 6odegpol_RectangleBoundTShapedNanoarray_Study01_RTATable.txt
13. 6odegpol_RectangleBoundTShapedNanoarray_Study03_RTATable.txt
14. 9odegpol_RectangleBoundTShapedNanoarray_Study00_RTATable.txt
15. 9odegpol_RectangleBoundTShapedNanoarray_Study01_RTATable.txt
16. 9odegpol_RectangleBoundTShapedNanoarray_Study02_RTATable.txt
17. 9odegpol_RectangleBoundTShapedNanoarray_Study03_RTATable.txt

File names containing:

- “odegpol” correspond to 0-rad linearly polarised light excitation.
- “3odegpol” correspond to $\pi/6$ -rad linearly polarised light excitation.
- “45degpol” correspond to $\pi/4$ -rad linearly polarised light excitation.
- “6odegpol” correspond to $\pi/3$ -rad linearly polarised light excitation.
- “9odegpol” correspond to $\pi/2$ -rad linearly polarised light excitation.
- “Study00” correspond to the 327.4-nm-by-247.5-nm rectangle-shaped nanostructure array. This nanostructure array acts as the bound for the remaining t-shaped structures in this folder.
- “Study01” correspond to the rectangle-bound 247.5 nm & 187.1 nm arms thicknesses t-shaped nanostructure array.
- “Study02” correspond to the rectangle-bound 247.5 nm & 143.0 nm arms thicknesses t-shaped nanostructure array.
- “Study03” correspond to the rectangle-bound 247.5 nm & 90.7 nm arms thicknesses t-shaped nanostructure array.

Section S8.4: Square-bound t-shaped nanostructure arrays

Nineteen .txt files are provided containing reflectance, transmittance, and absorptance data of square-bound nanostructure arrays excited by varying angles of linearly polarised light:

1. odegpol_SquareBoundTShapedNanoarray_Study00_RTATable.txt
2. odegpol_SquareBoundTShapedNanoarray_Study01_RTATable.txt
3. odegpol_SquareBoundTShapedNanoarray_Study02_RTATable.txt
4. odegpol_SquareBoundTShapedNanoarray_Study03_RTATable.txt
5. odegpol_SquareBoundTShapedNanoarray_Study04_RTATable.txt
6. 3odegpol_SquareBoundTShapedNanoarray_Study00_RTATable.txt
7. 3odegpol_SquareBoundTShapedNanoarray_Study01_RTATable.txt
8. 3odegpol_SquareBoundTShapedNanoarray_Study02_RTATable.txt
9. 45degpol_SquareBoundTShapedNanoarray_Study00_RTATable.txt
10. 45degpol_SquareBoundTShapedNanoarray_Study01_RTATable.txt

11. 45degpol_SquareBoundTShapedNanoarray_Study02_RTATable.txt
12. 60degpol_SquareBoundTShapedNanoarray_Study00_RTATable.txt
13. 60degpol_SquareBoundTShapedNanoarray_Study01_RTATable.txt
14. 60degpol_SquareBoundTShapedNanoarray_Study02_RTATable.txt
15. 90degpol_SquareBoundTShapedNanoarray_Study00_RTATable.txt
16. 90degpol_SquareBoundTShapedNanoarray_Study01_RTATable.txt
17. 90degpol_SquareBoundTShapedNanoarray_Study02_RTATable.txt
18. 90degpol_SquareBoundTShapedNanoarray_Study03_RTATable.txt
19. 90degpol_SquareBoundTShapedNanoarray_Study04_RTATable.txt

File names containing:

- “0degpol” correspond to 0-rad linearly polarised light excitation.
- “30degpol” correspond to $\pi/6$ -rad linearly polarised light excitation.
- “45degpol” correspond to $\pi/4$ -rad linearly polarised light excitation.
- “60degpol” correspond to $\pi/3$ -rad linearly polarised light excitation.
- “90degpol” correspond to $\pi/2$ -rad linearly polarised light excitation.
- “Study00” correspond to the 327.4-nm-by-327.4-nm square-shaped nanostructure array. This nanostructure array acts as the bound for the remaining t-shaped structures in this folder.
- “Study01” correspond to the square-bound 234.4 nm & 234.4 nm arms thicknesses t-shaped nanostructure array.
- “Study02” correspond to the square-bound 234.4 nm & 162.6 nm arms thicknesses t-shaped nanostructure array.
- “Study03” correspond to the square-bound 234.4 nm & 90.7 nm arms thicknesses t-shaped nanostructure array.
- “Study04” correspond to the square-bound 162.6 nm & 162.6 nm arms thicknesses t-shaped nanostructure array.

References

- [1] “COMSOL Multiphysics® v5.6.” COMSOL AB, Stockholm, Sweden, Nov. 11, 2020. [Online]. Available: www.comsol.com
- [2] “Wave Optics Module User’s Guide.” Stockholm, Sweden, 2020. Accessed: Jun. 05, 2023. [Online]. Available: <https://doc.comsol.com/5.6/doc/com.comsol.help.woptics/WaveOpticsModuleUsersGuide.pdf>
- [3] P. E. Ciddor, “Refractive index of air: new equations for the visible and near infrared,” *Appl. Opt.*, *AO*, vol. 35, no. 9, pp. 1566–1573, Mar. 1996, doi: 10.1364/AO.35.001566.
- [4] K. Luke, Y. Okawachi, M. R. E. Lamont, A. L. Gaeta, and M. Lipson, “Broadband mid-infrared frequency comb generation in a Si₃N₄ microresonator,” *Opt. Lett.*, *OL*, vol. 40, no. 21, pp. 4823–4826, Nov. 2015, doi: 10.1364/OL.40.004823.
- [5] G. Ghosh, “Dispersion-equation coefficients for the refractive index and birefringence of calcite and quartz crystals,” *Optics Communications*, vol. 163, no. 1, pp. 95–102, May 1999, doi: 10.1016/S0030-4018(99)00091-7.
- [6] T. Smith and J. Guild, “The C.I.E. colorimetric standards and their use,” *Trans. Opt. Soc.*, vol. 33, no. 3, p. 73, Jan. 1931, doi: 10.1088/1475-4878/33/3/301.
- [7] G. Sharma, *Digital Color Imaging Handbook*. 2003.
- [8] Internationale Beleuchtungskommission, Ed., “7.1 Calculation of tristimulus values,” in *Colorimetry*, 3rd ed.in CIE, no. 15. Wien: Comm. Internat. de l’éclairage, 2004, pp. 12–13.
- [9] Internationale Beleuchtungskommission, Ed., “11.4 Table T.4. CIE 1931 standard colorimetric observer,” in *Colorimetry*, 3rd ed.in CIE, no. 15. Wien: Comm. Internat. de l’éclairage, 2004, pp. 36–38.
- [10] “CIE Standard Colorimetric System,” in *Colorimetry*, John Wiley & Sons, Ltd, 2005, pp. 63–114. doi: 10.1002/0470094745.ch3.
- [11] Internationale Beleuchtungskommission, Ed., “11.1 Table T.1 Relative spectral power distributions of CIE illuminants,” in *Colorimetry*, 3rd ed.in CIE, no. 15. Wien: Comm. Internat. de l’éclairage, 2004, pp. 30–32.
- [12] Internationale Beleuchtungskommission, Ed., “7.3 Calculation of chromaticity coordinates,” in *Colorimetry*, 3rd ed.in CIE, no. 15. Wien: Comm. Internat. de l’éclairage, 2004, pp. 15–15.
- [13] M. D. Fairchild, “3.7 Chromaticity coordinates,” in *Color Appearance Models*, 2nd ed.England: John Wiley & Sons, 2005, pp. 77–78.
- [14] Internationale Beleuchtungskommission, Ed., “8.2.1 CIE 1976 (L*a*b*) colour space; CIELAB colour space,” in *Colorimetry*, 3rd ed.in CIE, no. 15. Wien: Comm. Internat. de l’éclairage, 2004, pp. 17–18.
- [15] M. D. Fairchild, “10.3 CIELAB,” in *Color Appearance Models*, 2nd ed.England: John Wiley & Sons, 2005, p. 185.
- [16] M. D. Fairchild, “4.6 Saturation,” in *Color Appearance Models*, 2nd ed.England: John Wiley & Sons, 2005, p. 88.
- [17] F. Schiller and K. R. Gegenfurtner, “Perception of saturation in natural scenes,” *J. Opt. Soc. Am. A, JOSAA*, vol. 33, no. 3, pp. A194–A206, Mar. 2016, doi: 10.1364/JOSAA.33.00A194.
- [18] F. Schiller, M. Valsecchi, and K. R. Gegenfurtner, “An evaluation of different measures of color saturation,” *Vision Research*, vol. 151, pp. 117–134, Oct. 2018, doi: 10.1016/j.visres.2017.04.012.
- [19] L. Hedjar, M. Toscani, and K. R. Gegenfurtner, “Perception of saturation in natural objects,” *J. Opt. Soc. Am. A, JOSAA*, vol. 40, no. 3, pp. A190–A198, Mar. 2023, doi: 10.1364/JOSAA.476874.
- [20] Internationale Beleuchtungskommission, Ed., “11.3 Table T.3 Tristimulus values, chromaticity coordinates of CIE illuminants,” in *Colorimetry*, 3rd ed.in CIE, no. 15. Wien: Comm. Internat. de l’éclairage, 2004, p. 35.

- [21] B. Auguié and W. L. Barnes, “Collective Resonances in Gold Nanoparticle Arrays,” *Phys. Rev. Lett.*, vol. 101, no. 14, p. 143902, Sep. 2008, doi: 10.1103/PhysRevLett.101.143902.
- [22] Dave Clements, “Conda 22.1.1 Release,” *Conda Community Forum*, Dec. 07, 2022. <https://conda.discourse.group/t/conda-22-11-1-release/139> (accessed Jul. 18, 2023).
- [23] Anaconda Inc., “Miniconda.” 2023. [Online]. Available: <https://docs.conda.io/en/latest/miniconda.html>
- [24] Anaconda Inc., “Anaconda Software Distribution.” 2023. [Online]. Available: <https://docs.anaconda.com/>
- [25] Guido van Rossum and The Python development team, “The Python Language Reference Release 3.10.12.” Jul. 02, 2023. [Online]. Available: <https://docs.python.org/3.10/reference/index.html>
- [26] Python Software Foundation, “Python Release Python 3.10.8,” *Python.org*, Oct. 11, 2022. <https://www.python.org/downloads/release/python-3108/> (accessed Jul. 18, 2023).
- [27] Colour Developers, “Colour.” Nov. 29, 2022. [Online]. Available: <https://colour.readthedocs.io>
- [28] T. A. Caswell *et al.*, “matplotlib/matplotlib: REL: v3.6.2.” Zenodo, Nov. 03, 2022. doi: 10.5281/zenodo.7275322.
- [29] J. D. Hunter, “Matplotlib: A 2D Graphics Environment,” *Computing in Science & Engineering*, vol. 9, no. 3, pp. 90–95, May 2007, doi: 10.1109/MCSE.2007.55.
- [30] “NumPy 1.23.5 Release Notes — NumPy v1.25 Manual,” Nov. 19, 2022. <https://numpy.org/doc/stable/release/1.23.5-notes.html> (accessed Jul. 18, 2023).
- [31] C. R. Harris *et al.*, “Array programming with NumPy,” *Nature*, vol. 585, no. 7825, Art. no. 7825, Sep. 2020, doi: 10.1038/s41586-020-2649-2.
- [32] The pandas development team, “pandas-dev/pandas: Pandas.” Feb. 2020. [Online]. Available: <https://doi.org/10.5281/zenodo.3509134>
- [33] W. McKinney, “Data Structures for Statistical Computing in Python,” presented at the Python in Science Conference, Austin, Texas, 2010, pp. 56–61. doi: 10.25080/Majora-92bf1922-00a.
- [34] M. L. Waskom, “seaborn: statistical data visualization,” *Journal of Open Source Software*, vol. 6, no. 60, p. 3021, Apr. 2021, doi: 10.21105/joss.03021.
- [35] Anaconda Inc., “Managing environments — conda 23.5.3.dev84 documentation,” *Conda - conda 23.5.3.dev84 documentation*, 2023. <https://conda.io/projects/conda/en/latest/user-guide/tasks/manage-environments.html#activating-an-environment> (accessed Jul. 18, 2023).
- [36] sil2100, “Jammy Jellyfish Release Notes,” *Ubuntu Community Hub*, Jun. 15, 2023. <https://discourse.ubuntu.com/t/jammy-jellyfish-release-notes/24668> (accessed Jul. 18, 2023).
- [37] craigloewen-msft, “Install Linux on Windows with WSL,” *Microsoft Learn*, Jan. 12, 2023. <https://learn.microsoft.com/en-us/windows/wsl/install> (accessed Jul. 18, 2023).
- [38] Wolfram Research, Inc., “Mathematica.” Champaign, Illinois, 2023. Accessed: Jul. 20, 2023. [Online]. Available: <https://www.wolfram.com/mathematica/>
- [39] “Launching Version 13.0 of Wolfram Language & Mathematica—Stephen Wolfram Writings,” Dec. 13, 2021. <https://writings.stephenwolfram.com/2021/12/launching-version-13-0-of-wolfram-language-mathematica/> (accessed Jul. 20, 2023).
- [40] “CIE 1931 colour-matching functions, 2 degree observer,” International Commission on Illumination, 2019. doi: 10.25039/CIE.DS.xvudnb9b.
- [41] International Commission On Illumination (Cie), “CIE standard illuminant D65.” International Commission on Illumination (CIE), 2022. doi: 10.25039/CIE.DS.hjfm59.